Dynamic carbon and sulfur cycling in the aftermath of the Lomagundi-Jatuli Event: Evidence from the Paleoproterozoic Hutuo Supergroup, North China Craton

(*to be submitted to Precambrian Research*)

Guang Ouyang[a, b], Zhenbing She[a*, b], Dominic Papineau[a*, c, d, e], Xiangfa Wang[b], Genming Luo[a, b], Chao Li [a]

a State Key Laboratory of Biogeology and Environmental Geology, China University of Geosciences, Wuhan 430074, China

b School of Earth Sciences, China University of Geosciences, Wuhan, 430074, China

c Department of Earth Sciences, University College London, Gower Street, London WC1E 6BT, UK

d London Centre for Nanotechnology, 17-19 Gordon Street, University College London, London, UK

e Centre for Planetary Science, University College London

Abstract

The unprecedented positive $\delta^{13}C$ excursion in carbonates between 2.2 to 2.0 Ga, known as the Lomagundi-Jatuli Event (LJE), has been documented globally and linked to the rise of atmospheric oxygen . Increasing oxidation inevitably changed the atmosphere-hydrosphere system, but few chemostratigraphic or quantitative constraints for the aftermath of this event exists. Here we describe a ~200 m-thick carbonate succession in the Huaiyincun Formation, Hutuo Supergroup, ~2.0-1.9 Ga, from the North China Craton. There is a lithological transition from pink-purple dolostones to grey dolostones at ca. 91.6 m above the base of the Huaiyincun Formation. The former are more enriched in hematite and outsized detrital minerals, whereas the latter contain more organic matter but almost no detrital phases. Meanwhile, the frequent occurrence of tempesite structures, along with the abrupt decline of stromatolites in the upper Huaiyincun Formation, suggest a storm-dominated environment. These distinct features within the Huaiyincun Formation reveal increased water depth during a transgression event. Two types of Raman spectra of organic matter were found in the lower and upper Huaiyincun Formation, respectively, which is proposed to be the result of variable oxidation.

At 65.6m, 26m below the lithological transition (~91.6m), remarkable decreases in both $\delta^{13}C_{carb}$ and $\delta^{34}S_{CAS}$ are observed. This discordance between C-S isotopic excursions and sedimentological and mineralogical variations argues against a seawater depth gradient effect of the $\delta^{13}C_{carb}$ and $\delta^{34}S_{CAS}$ curves. Instead, the decline of $\delta^{13}C_{carb}$ rather correlates with the negative $\delta^{13}C$ excursions in ca. 2.0 Ga carbonates from Gabon and Russia, known as the Shunga-Francevillian Event (SFE). The result of the quantitatively constrained paleo-seawater $[SO_4^{2-}]_{sw}$ suggests a crash in the seawater sulfate reservoir compared with that during the preceding LJE. However, the decreased $\delta^{34}S_{CAS}$ and increased CAS concentration towards the top of the study unit represent the recovery of seawater sulfate reservoir. The coordinated decline in $\delta^{34}S_{CAS}$ and $\delta^{13}C_{carb}$ values is likely related to enhanced oxidation of continental pyrite and organic matter in the aftermath of the LJE. The Huaiyincun Formation therefore represents a critical interval that recorded dynamic carbon and sulfur cycles after the LJE.

Keywords: Hutuo Supergroup, transgression, carbon isotope, carbonate-associated sulfate (CAS), North China Craton

1. Introduction

Carbonates with anomalously high $\delta^{13}C$ values were first discovered in the Paleoproterozoic successions of the Lomagundi Group in Zimbabwe and the Jatuli Group in Fennoscandia (Galimov et al., 1968; Schidlowski et al., 1975). Since then, similarly high values (>5‰) of $\delta^{13}C$ have been reported from carbonates in coeval successions world wide (Bekker et al., 2006; Lindsay and Brasier, 2002; Melezhik and Fallick, 2010; Préat et al., 2011). This unprecedented perturbations in carbon isotope composition was thereby recognized as a worldwide event termed as the Lomagundi-Jatuli event (Schidlowski et al., 1976; Melezhik et al., 2005), ended by the return of $\delta^{13}C$ values to near 0‰ after 2060 Ma (Karhu et al., 1996; Martin et al., 2013b). The termination and aftermath of these unprecedented perturbations in the carbon cycle was represented by dramatic changes of $\delta^{13}C$ from positive to negative values in the 2090-1980 Ma Zaonega Formation in the Onega paleo-basin and the 2083-2050 Ma Francevillian Series of Gabon (Kump et al., 2011; Melezhik et al., 2015; Ossa Ossa et al., 2018). This was recognized as the Shunga-Francevillian Event (SFE), likely to have resulted from massive oxidation of organic matter (OM) (Kump et al., 2011). While the global nature of this negative carbon isotope excursion remains to be confirmed, little effort has been paid to decipher their local responses in various sedimentary environments. More of multiple geochemical proxies with solid petrographic context are needed for a thorough understanding of the dynamic biogeochemical cycles in the post-LJE oceans.

Oceanic sulfate plays a key role in biogeochemical C cycle through bacterial sulfate reduction (Berner, 1989). Sulfur isotopes in sedimentary rocks have been widely used to explore the oxidative weathering, to quantify the seawater sulfate levels and to constrain paleo redox states of the oceans (Algeo et al., 2015； Canfield and Teske, 1996; Guo et al., 2015; Luo et al., 2015,2016; Papineau et al., 2007； Shi et al., 2018). A number of attempts have been made to reconstruct Paleoproterozoic seawater sulfate concentrations and their connections with the redox state of the atmosphere and hydrosphere (Bottrell and Newton, 2006; Habicht, 2002; Luo et al., 2015, 2010; Planavsky et al., 2012; Scott et al., 2014). Growing evidence shows that $[SO_4^{2-}]_{sw}$ during the LJE has greatly increased and probably reached a maximum value of 10mM at the falling limb of the LJE (Blättler et al., 2018), as a result of the massive oxidative weathering of continental sulfides (Konhauser et al., 2011; Planavsky et al., 2012). In stark contrast to the remarkable expansion of sulfate reservoir during the LJE, $[SO_4^{2-}]_{sw}$ in the late Paleoproterozoic and early Mesoproterozoic is estimated to be lower than 2.5mM (Kah et al., 2004; Gellatly et al., 2005) or even much lower than 1 mM (Luo et al., 2015; Fakhraee et al., 2019). Pyrite multiple-sulfur isotopic data support a rapid expansion of the seawater sulfate reservoir (SSR) during the Great Oxidation Event (GOE) at ca. 2.3 Ga followed by a subsequent contraction in the size of the reservoir at ca. 2.05 Ga (Scott et al., 2014). Details of the transition from expansion to contraction, however, remain obscure and require detailed investigations of coeval successions elsewhere.

Shifts of $\delta^{13}C_{carb}$ value from +3.4‰ to < -3‰ have been documented in the carbonates of the 2.14-1.83 Ga Hutuo Supergroup in the North China Craton (Kong et al., 2011; She et al., 2016; Zhong and Ma, 1995), similar to those on other continents (Kump et al., 2011; Melezhik et al., 2015; Ossa Ossa et al., 2018). It has been interpreted as the result of a deglaciation event (Kong et al., 2011), or corresponding to the onset of the SFE (She et al., 2016). Here we present high-resolution stratigraphic carbon and sulfur isotope data, combined with detailed sedimentology and petrography of Paleoproterozoic carbonates from the Huaiyincun Formation, Hutuo Supergroup in the North China

Craton. The coupled $\delta^{13}C_{carb}$, $\delta^{13}C_{org}$ and $\delta^{34}S_{CAS}$ data of the Huaiyincun Formation shed new light on the critical period between the LJE and the SFE.

2. Geological setting

The North China Craton is one of the oldest cratonic blocks in the world that can be divided into the Eastern and Western blocks, separated by the Trans-North China Orogen (Fig. 1a) (Zhao et al., 2001). Paleoproterozoic volcano-sedimentary successions are widespread in the North China Craton (Kusky and Li, 2003), the most representative of which being the Hutuo Supergroup. The Hutuo Supergroup is part of the Trans North China Orogen and is located in the Wutai area, Shanxi Province (Fig. 1a). The thickness of the supergroup is estimated to be more than 10,000 m, and the rocks have only been metamorphosed to the sub-greenschist facies (Bai, 1986; Du et al., 2011). The base of the Hutuo Supergroup sits unconformably on the Neoarchean Gaofan and Wutai Groups. The Gaofan Group consists of fine-grained terrestrial clastic rocks that are metamorphosed to the greenschist facies (Bai, 1986), whereas the Wutai Group is a sedimentary-volcanic sequence dominated by greenschist to lower amphibolite facies metamorphic rocks (Peng et al., 2017). Bai (1986) divided the Hutuo Supergroup from bottom to top into 3 groups (Fig. 1b), the Doucun, Dongye and Guojiazai groups which were further subdivided into 14 formations (Fig. 1a). The Doucun Group unconformably overlies the Neoarchean Wutai Group, and was subdivided into the Sijizhuang, Nantai, Dashiling and Qingshicun formations. Recent discovery of striated and faceted boulders and dropstones in sandstones and siltstone-mudstone facies of the lowermost Sijizhuang Formation suggest that the deposition of the Hutuo Supergroup probably started with a deglaciation event (Chen et al., 2019). The presence of continental flood basalt and bimodal volcanics and the change from coarse clastic sediments into fine-grained siliciclastic rocks has been well recognized in the Doucun Group, suggesting a rift-related environment during the crustal extension (Bai, 1986; Kusky and Li, 2003). Unconformably overlying the Doucun Group, the Dongye Group includes massive dolostones of the Qingshicun, Wenshan, Hebiancun, Jianancun, Daguandong, Huaiyincun, Beidaxing and Tianpengnao formations (Li et al., 1996). These formations are dominated by thick bedded dolomite sequence with intercalation of metapelite and metabasalt. The Huaiyincun Formation is overlained by the Beidaxing Formation which is characterizied by grey dolomicrite. The Daguandong Formation underlying the Huaiyincun Formation consists of dark-grey dolomicrite intercalated with greyish-green slate. Stromatolites with diverse domal and columnar morphologies are found throughout the Dongye Group except for the Huaiyincun Formation with only minor stromatolitic content (Bai, 1986). Upward in the succession, the Dongye Group is unconformably overlain by the Guojiazhai Group, a non-marine molasse deposits which has been further subdivided into Xiheli, Heibeishan and Diaowangshan Formations (Bai, 1986).

The depositional age of the Hutuo Supergroup has been constrained by previous geochronological studies on sandstones and metavolcanic interbeds (Fig. 1b) (Du et al., 2011, 2010; Liu et al., 2011; Peng et al., 2017; Wan et al., 2010; Wilde et al., 2004). A group of zircons in basaltic andesite from the bottom of the Sijizhuang Formation yielded a weighted mean $^{207}Pb/^{206}Pb$ age of 2140±14 Ma, which set the maximum age for the base of Hutuo Supergroup (Du et al., 2010). Detrital zircon geochronological work on the Guojiazhai Group produced youngest ages between 1.96-1.92 Ga (Liu et al., 2011; Du et al., 2011). Considering the fact that the Guojiazhai Group is older than its cross-cutting late Paleoproterozoic mafic dykes (1.78–1.75 Ga; Peng et al., 2005) and the overlying Changcheng Group, Du et al (2017)

suggested that the Guojiazhai Group deposited between 1.9-1.8 Ga, constraining the upper limit of the age of the Hutuo Supergroup. Direct constraint for the age of the Huaiyincun Formation, however, is lacking, because the formation consists exclusively of carbonate rocks. Sixty four detrital zircons from the underlying Wenshan Formation yield a $^{207}Pb/^{206}Pb$ weighted mean age of 2068±3Ma (Du et al., 2011). A mafic sill intruding the Qingshicun Formation gives a 2057±25 Ma zircon U-Pb age (Peng et al., 2017). Metasandstones collected from the Hebiancun Formation contain a youngest group of zircons with ages around 2010 Ma (Liu et al., 2011), indicating the deposition of the overlying Huaiyincun Formation is later than 2.0 Ga. Collectively, available data suggest that the deposition age of the Huaiyincun Formation can be roughly constrained between 2.0 and 1.9 Ga.

3. Sedimentary features

The Huaiyincun Formation is well exposed at the Huaiyincun East section (GPS coordinates 38°39'22.09"N, 113° 7'31.82"E), ca. 1.5 km northwest of Dongye Town (Fig. 1a). It conformably overlies the Daguandong Formation (Fig. 2a-b) and starts with dolostone intercalated with purple metapelite (Fig. 2c). The Huaiyincun Formation is characterized by non-stromatolitic dolostone, with only a few beds of stromatolitic bioherm occurring at ca. 15 m above the base (Fig. 2d). At about 91.6m above the base of the Huaiyincun Formation, a notable lithological transition from pink dolostone to grey dolostone occurs (Fig. 3a-b), marking the boundary between the lower and the upper parts of the formation. The lower Huaiyincun Formation consists of laminated or banded dolostone (Fig. 3c), with subordinate occurrence of intraclastic dolostone (Fig. 3d). The upper Huaiyincun Formation, however, is dominated by intraclastic dolostone, consisting of dolomitic intraclasts with variable sizes from calcarenite to calcirudite (Fig. 3e-f). Frequent occurrence of hummocky cross-stratification (Fig. 3g), and decimeter-thick cycles from normally-graded dolomitic calcarenite to calcirudite (Fig. 3f) are observed in the upper Huaiyincun Formation.

4. Samples and methods

Thirty-four dolostone samples were collected from the ca. 200m interval of the Huaiyincun Formation in this study. All samples were selected from fresh outcrop to minimize the impact of weathering. Weathered surfaces and veins were cut off during sample preparation. For comparison, two samples of organic-rich metapelites from the Gaofan Group and a sample of banded iron formation (BIF) from the Wutai Group were also collected.

Thin sections were prepared using conventional methods, ground to 30 microns thickness and polished. They were cleaned with distilled water to remove surface contaminants. Petrographic characterization of thin sections was conducted with two petrographic microscopes (a Zeiss Axio Scope A1 at CUG-Wuhan and an Olympus BX51 at UCL) equipped with 5X, 10X, 20X, 50X and 100X objectives under the transmitted and reflected light. Photomicrographs were taken under AxioVision LE64 imaging system and the Stream Start software that controls the UC50 (5 mega pixels) CCD camera.

Micro-Raman imaging was conducted at the London Centre for Nanotechnology at UCL with a WITec α300 confocal Raman imaging system. A 532 nm laser was used with a power between 7 and 10 mW and focused with a 50X or 100 X objective for both large and small area scans, achieving spatial

resolutions between 2000 and 360 nm. Each pixel collected a Raman spectrum with a typical dwell time of 0.5s. A 50 micron diameter optic fiber was selected as a compromise for confocality and signal-to-noise ratio and a 600 grove/mm grating was used to provide a large bandwidth of 4000cm^{-1} and a spectral resolution of 4 cm^{-1}. The targets for Raman imaging were examined under the reflected light to exclude areas of open cavities and popped-out grains that could have captured contaminants from polishing. The analyses were performed at least 0.5μm below the sample surface to rule out potential contamination on the sample surface. All Raman spectra herein were generated by averaging pixels with nearly identical spectra and processed with WITec Project FOUR 4.0. Cosmic rays were removed under 2cm^{-1} filter with dynamic factor of 8. Then the background was subtracted by using polynomial functions with up to the 7th order. Minerals are shown coded in different colors according to their characteristic peaks. Deconvolution of Raman peaks of OM (D1, D2, D3, D4 and G) was performed using linear combinations of the Lorentz function. Temperatures are estimated after Beyssac et al (2002) according to applicable range of temperature.

For bulk geochemical analyses, fresh dolostone specimens were crushed into mm-sized chips and handpicked to remove secondary veinlets and weathered surfaces. The rock chips were ultrasonically cleaned with distilled water and oven-dried at 50◦C before powdering in a shatter box with tungsten carbide puck mill. Glass were shattered between each sample to make sure no residue stick on the mill, then the mill was cleaned with distilled water and ethanol between each sample.

The oxygen and carbon isotope ratios of carbonates ($\delta^{13}C_{carb}$ and $\delta^{18}O_{carb}$) were determined at the State Key Laboratory of Biogeology and Environmental Geology, China University of Geosciences (Wuhan). The analytical procedures followed previously described technique (Song et al., 2014), for which 150-400μg of powdered samples were sealed in exetainers with a butyl rubber septum, and reacted with 100% phosphoric acid at 72°C after flushing the head space with helium. The evolved CO_2 gas was analyzed for $\delta^{13}C$ and $\delta^{18}O$ using a MAT 253 mass-spectrometer coupled directly to a Finnigan Gasbench II interface (Thermo Scientific). External reproducibility was better than 0.06‰ for $\delta^{13}C$ and 0.1‰ for $\delta^{18}O$ ($\cdot 1\sigma$) based on replicate analyses of two laboratory marble and calcite standards (GBW 04416 and GBW 04417). Analytical precision is better than 0.02‰ for $\delta^{13}C$ and 0.06‰ for $\delta^{18}O$.

For the determination of carbon isotope ratios of organic carbon ($\delta^{13}C_{org}$), 2g of sample powder was decarbonated with 6 M HCl for 12h. The residue was rinsed with deionized water until neutral pH was achieved, then centrifuged and freeze-dried for 24 h. Decarbonated sample powders of the low TOC samples from the lower Huaiyincun Formation were treated with HF for removal of silicates, rinsed with deionized water and dried. Sample powders (typically 0.1 to 0.2 g) were mixed with CuO powder, and a piece of Pt wire and were loaded into a quartz tube. The tubes were evacuated, sealed and combusted at 850◦ for 4h. The resulting CO_2 was cryogenically isolated and sealed in glass tubes for $\delta^{13}C_{org}$ analysis. The CO_2 was analyzed using a Finnigan MAT 251 isotope-ratio mass spectrometer (IRMS) at the State Key Laboratory of Geological Processes and Mineral Resources in China University of Geosciences using the GBW04407 ($\delta^{13}C$ =−22.4‰) and GBW04408 ($\delta^{13}C$ =−36.9‰) (China national standards) as the calibrating standards. Replicate analyses of the standards gave an external reproducibility of 0.3‰ ($\cdot 1\sigma$). Analytical precision is better than 0.06‰.

The extraction of carbonate-associated sulfate (CAS) followed the procedure of Thompson and Kah (2012). Due to the generally low concentrations of CAS in Precambrian dolostones, 200g of each sample was used during the extraction. The powdered samples were immersed in 10% NaCl solution for 24 hours, and supernatant was pumped out to remove OM and soluble sulfate. The supernatant was tested

with $BaCl_2$ solution (250g/L) to make sure that soluble sulfate has been completely removed. The insoluble substance was leached three times with deionized water. After addition of 3 mol/L hydrochloric acid, the solution was stirred and kept at pH<2 during the reaction. The solution was then filtered with glass fiber filter with pore size of 0.45μm. Approximately 200ml of 250g/L $BaCl_2$ solution was then added to the percolate to precipitate the sulfate as $BaSO_4$. Finally, the $BaSO_4$ precipitates were dried, weighed, and prepared for sulfur isotope analyses. CAS concentrations were calculated through the mass of sulfate radical in the $BaSO_4$ precipitates and the samples used in extraction.

Sulfur isotope ratios of CAS ($\delta^{34}S_{CAS}$) were measured at the State Key Laboratory of Biogeology and Environmental Geology, China University of Geosciences (Wuhan). Barium sulfate precipitates were homogenized, combined with an excess amount of V_2O_5, and analyzed using a Finnigan MAT 252 gas source mass spectrometer fitted with an elemental analyzer for on-line sample combustion. All sulfur isotope compositions are expressed in standard delta notation as per mil (‰) deviations from Vienna Canyon Diablo Troilite (V-CDT). NBS 127 (20‰), IAEA S05 (0.5‰) and IAEA S06 (-34.1‰) are using as the calibrating standards based on 8 replicate analyses. The average values are 20.1‰, 0.5‰ and -34.1‰, and standard deviations are less than 0.2‰.

5. Result

5.1 Mineralogy

Mineral assemblage of the carbonate rocks is characterized by dolomite + quartz + muscovite + feldspar throughout the Huaiyincun Formation, based on petrographic observations of 34 samples. The lower Huaiyincun Formation (below 91.6m) has abundant hematite disseminations and sometimes hematite films coating carbonates or other minerals such as zircons (Fig. 4b, c, f). Large grains of detrital minerals such as feldspar, quartz, rutile, anatase, and rounded apatite > 20μm in diameter are also found in the lower Huaiyincun Formation (Fig. 4b-ce-f), but are absent from the overlying grey dolostone (above 91.6m) (Fig. 4h-i, k-l). The amount of disseminated hematite is greatly reduced in the upper Huaiyincun Formation (Fig. 4l), where it sometimes occurs as fracture-filling (Fig. 4h). Moreover, the lower abundances of hematite in the upper Huaiyincun Formation apparently corresponds to relative enrichment of OM (Fig. 4c, f) compared with samples of the lower Huaiyincun Formation (Fig. 4i, l).

5.2 Raman spectroscopy of OM

On the basis of analyses of 30 samples in the Huaiyincun Formation (4 samples have no Raman signal of organic matter), two different types of Raman spectra for OM are identified by the FWHM (full width at half maximum) of peaks and D/G band positions (Fig. 5, Table 2) In the lower Huaiyincun Formation, the spectra of OM are characterized by a broad D1 peak (FWHM = 244cm^{-1}) located at 1350 cm^{-1} and a G band (FWHM = 79cm^{-1}) at 1580 cm^{-1}. In the upper Huaiyincun Formation, however, the spectra display a narrow and intense D1 band (FWHM = 51cm^{-1}) located at 1352 cm^{-1} whereas the G band is located at 1599cm^{-1} (FWHM = 48cm^{-1}). Moreover, a weak 2D band at around 2964 cm^{-1} is clearly visible in the upper Huaiyincun samples, but absent in the lower Huaiyincun samples.

Raman spectra of graphite from the Gaofan Group, an OM-rich succession unconformably underlying the Hutuo Supergroup, are characterized by a much narrower D1 band at 1361± 1cm^{-1} (FWHM = 43 and 64cm^{-1}) and a more prominent G band (FWHM = 20 and 23cm^{-1}) centered at 1587± 1cm^{-1}. Raman spectra of graphite from a BIF succession of the Wutai Group, are also characterized by D1 band at around 1342cm^{-1} (FWHM = 60cm^{-1}) and narrow G band (FWHM = 23cm^{-1}) centered at around 1578cm^{-1}.

5.3 C isotopes of carbonate and OM

$\delta^{13}C_{carb}$ and $\delta^{18}O$ values measured in this study (n_T=36, including 2 duplicates) and from She et al. (2016) (n_S=10, data were selected based on carefully stratigraphical correlation) of the 194-m thick Huaiyincun Formation range between +1.5‰ and -3.7‰ V-PDB (n=46), with an average of -2.0‰ (Table 1, Fig. 6), whereas the $\delta^{18}O$ values range between -6.1‰ and -9.7‰ with an average of -8.6‰. Two stages can be recognized in the $\delta^{13}C_{carb}$ curve. $\delta^{13}C_{carb}$ values ranging between +1.4‰ to -0.3‰ are observed in the lower part of the formation (0-65.6m), with an average of 0.2‰. From 65.6m to 82.5m, $\delta^{13}C_{carb}$ values show an abrupt decrease from -0.1‰ to -3.7‰ within 16.9m. Starting from 82.5 m, the $\delta^{13}C_{carb}$ values are persistently negative, showing a slightly, but systematically increasing trend from -3.4 to -2.3‰.

Values of $\delta^{13}C_{org}$ range between -26.0‰ and -28.9‰, with an average of -27.8‰ (n=27, including 1 duplicate). Generally, $\delta^{13}C_{org}$ co-varies with $\delta^{13}C_{carb}$ (Fig. 6), with a $\Delta^{13}C$ ($\delta^{13}C_{carb}$ -$\delta^{13}C_{org}$) of 27.7‰ – 24.1‰ (Table 1). A slightly decreasing tendency is observed below 71m, which corresponds to the decrease in $\delta^{13}C_{carb}$ values (Fig. 6). The TOC of carbonate rocks in the Huaiyincun Formation is 0.02‰ and lower.

5.4 Concentration and S isotopes of carbonate-associated sulfate (CAS)

CAS concentrations of the carbonate rock in the upper Huaiyincun Formation ranges from 2.76 to 28.09 ppm (Table 1) with an average value of 15.39 ppm (n=15), displaying an overall increasing trend (Fig. 6). For samples below 135.5 m in the section, the amount of precipitated $BaSO_4$ was too small to be precisely weighed and therefore the CAS concentration was not determined. The generally low CAS level, however, did not affect the determination of $\delta^{34}S_{CAS}$ because the required amount of sulfate is at the µg level. Values of $\delta^{34}S_{CAS}$ of the Huaiyincun dolostones fluctuate between +33.1‰ and -1.2‰ (Table 1) with an average of +15.3‰ (n=27, including 1 duplicate). The decline in $\delta^{34}S_{CAS}$ is observed starting at 65.6m with the highest value of 33.1‰, followed by a generally decreasing trend through most of the upper Huaiyincun Formation (Fig. 6).

6.Discussion

6.1 A transgressional event recorded in the Huaiyincun Formation

Previous studies have suggested that the Huaiyincun Formation represented a period of maximum transgression in the Hutuo Supergroup (Bai, 1986). Our observations, however, document more details of the depositional environment for the Huaiyincun Formation. In contrast to the underlying Daguandong Formation, which consists of abundant stromatolites (Fig. 2e), only a few beds of stromatolites are found in the Huaiyincun Formation. The imbricated edgewise intraclasts in the lower Huaiyincun Formation (Fig. 3d) point to a proximal deposition at the storm surge. Further upsection, frequent occurrences of hummocky cross-stratification (Fig. 3g) suggest deposition between the storm wave base and the fair weather wave base. In the upper Huaiyincun Formation, repeated occurrences of decimeter-thick cycles from normally graded calcarenite to calcilutite (Fig. 3f) are consistent with deposition of older carbonate rock eroded by storm (dolomitic detritus) on a carbonate ramp below the storm wave base, suggesting an increase in water depth. The abrupt decline of stromatolites and the dominance of storm-induced deposition are consistent with a prominent transgression which led to the drowning of the Hutuo carbonate platform.

Mineralogy of the Huaiyincun carbonates reveals further changes in depositional environments across the Huaiyincun Formation (Fig. 4). Compared with the upper Huaiyincun Formation, the pink dolostone in the lower Huaiyincun Formation contains more detrital phases derived from continental weathering. The enrichment of hematite and the absence of pyrite in the lower Huaiyincun Formation reveal an oxidized shallow marine environment. This is consistent with higher iodine concentration in some Paleoproterozoic carbonates, which suggests that a shallow marine oxycline persisted through the Proterozoic Eon (Hardisty et al., 2017). By contrast, the upper Huaiyincun Formation is characterized by lower abundance of hematite (Fig. 4). This transition from dolostone rich in hematite and detrital minerals to those with less detrital phases and hematite, is consistent with the interpretation from sedimentology of a transgression to a deeper and less oxidizing marine environment.

In summary, sedimentological and mineralogical features suggest an overall increase in water depth from the lower part to the upper part of the Huaiyincun formation. This transgression likely resulted in a transition to less oxidizing water column and hence the color change from pink to grey in the dolostones. The frequent occurrence of storm-related sediments also suggests an depositional environment connected with the open ocean for the Huaiyincun Formation, which has likely captured signals of global biogeochemical changes after the LJE.

.

6.2 Authigenicity and variable oxidation of OM

TiO_2 minerals, apatite and quartz have been observed in association with microfossils and mineralised biomass in barite and chert (Djokic et al., 2017; Papineau et al., 2017), although these kinds of minerals can be either authigenic or detrital in origin. In the lower Huaiyincun dolostones, large grains of TiO_2 mineral, apatite and quartz are usually rounded (Fig. c, f), suggesting that they are detrital minerals that have been transported over a distance before their final deposition. By contrast, detrital content is much lower in the grey dolostones of the upper Huaiyincun Formation, whereas OM particles are more enriched (Fig. 4i, l). The negative correlation of detrital and OM contents, along with the fact

that OM in the Huaiyincun samples mainly occurs as disseminations in dolomites (Fig. 4i, j; Fig. 5a-b, d-e), are consistent with an authigenic origin for the OM.

Metamorphic temperatures were calculated on the basis of the empirical Raman thermometer calibrated with carbonaceous material in metasediments from Western Alps (Beyssac et al., 2002). Raman spectra of the OM in the Huaiyincun Formation yield peak metamorphic temperatures between 327 and 337°C (Table 2),. These features are distinctly different from those of the Gaofan and Wutai samples (Fig. 5g) which yield significantly higher peak metamorphic temperatures, ranging between 417 to 507℃ (Table 2). The prominent G-band at ca. 1590 cm^{-1} and much less intense D-band of OM in the Gaofan and Wutai groups suggest a higher degree of thermal maturation, consistent with a metamorphic grade of the greenschist facies to lower amphibolite facies derived from mineral assemblages (Bai, 1986; Peng et al., 2017). These observations can be used to exclude the possibility that the Huaiyincun OM is detrital in origin, and it is not derived from older OM-bearing successions. Moreover, the main mineral assemblages and microstructures do not show significant changes within the whole Huaiyincun Formation, indicating that all the Huaiyincun dolostones underwent the same grade of metamorphism, and that the Raman spectral variations of the OM were caused by different thermal maturation is unlikely. Although graphite crystals can produce Raman spectra with different ratios of D and G band intensities depending on the incident angle of laser (Beyssac et al., 2003; Wang, 1989), it cannot account for the difference in FWHM and the distinct Raman spectra of the Huaiyincun OM. Hence, the two types of OM in the Huaiyincun Formation are both primary OM and their spectral differences are not related to differential thermal maturation or orientation of graphite domains. Recent Raman spectroscopic studies of graphitic carbons associated with apatite in a range of metamorphosed Precambrian Banded Iron Formations show that more than one type of OM crystallinity can occur in individual rocks, sometimes within only a few microns distance (Dodd et al., 2019). It is thus possible that the two types of OM result from variable oxidation, whereby more prominent D1 peaks represent higher levels of functional groups, or from different sources of primary OM from the depositional environment.

6.3 Impact of post-depositional processes on C and S isotope compositions

During post-depositional processes such as metamorphism and diagenesis, original carbon and oxygen isotope signals of carbonate rocks could either be altered at various degrees (e.g., Bickle et al., 1997), or retained even under the amphibolite-facies conditions (e.g., Baker and Fallick, 1989a, b). It has been shown that diagenesis tend to result in a decrease in both $\delta^{13}C_{carb}$ and $\delta^{18}O_{carb}$ (Bekker et al., 2006; Melezhik and Fallick, 2010), which led to the use of the co-variation of $\delta^{13}C_{carb}$ and $\delta^{18}O_{carb}$ as an indicator of post-depositional alteration of C and O isotope compositions. However, the carbon isotope system of carbonate is strongly buffered to the primary $\delta^{13}C$ signal because the abundance of carbon in pore water and diagenetic fluids is much lower than that in carbonates (Banner and Hanson, 1990). Therefore, carbon isotope composition of most of the bulk rock samples is unlikely to change significantly during diagenesis and metamorphism. As shown in Fig. 7a, there is no correlation between $\delta^{13}C_{carb}$ and $\delta^{18}O_{carb}$ in our samples of the Huaiyincun samples, suggesting that the C-O isotopic systematics is unlikely affected by post-sedimentary processes.

There are concerns about laboratory-introduced artifacts or post-depositional alteration regarding the S isotope of CAS. Studies have shown that pyrite oxidation can occur during the extraction of CAS (Marenco et al., 2008; Mazumdar et al., 2008). Powders of our samples were completely dissolved with

3 M HCl, and solutions were kept at pH < 2 during the reaction to minimize pyrite oxidation (Thompson and Kah, 2012). Furthermore, no pyrite has been found in the studied samples through petrographic observations and Raman imaging (Fig. 2 and 4). The absence of co-variation between $\delta^{34}S_{CAS}$ and CAS (Fig. 7c) concentration further excludes the possibility of CAS contamination by the oxidation of pyrite during extraction (Marenco et al., 2008; Mazumdar et al., 2008). The very low contents of CAS with extremely high $\delta^{34}S$ values can also exist in carbonates precipitated in methanic zone (Planavsky et al., 2012). However, neither anomalously positive $\delta^{13}C_{carb}$ nor the correlation between $\delta^{34}S_{CAS}$ and $\delta^{13}C_{carb}$ were found within the Huaiyincun Formation (Fig. 7d). Besides, the generally high $\delta^{13}C_{org}$ values are inconsistent with the large negative excursions related to methanogenesis. The potential effect of methanic environment can therefore be excluded. The impact of diagenetic overprint on CAS has been studied by Fichtner et al (2017). The result revealed that the $\delta^{34}S_{CAS}$ withstands burial diagenesis, and reliably preserved the record of ambient seawater sulfate. The exchange between CAS and carbonate at temperatures of >200℃ would increase the $\delta^{18}O_{CAS}$ values, which would cause decrease in $\delta^{18}O_{carb}$ values. Thus, although a weak correlation between $\delta^{34}S_{CAS}$ and $\delta^{18}O_{carb}$ is observed (Fig. 7b), we consider the $\delta^{34}S_{CAS}$ values of carbonate rocks in the Huaiyincun Formation reflect primary seawater values. Also, despite meteoric diagenesis and dolomitization in carbonate rock, it has been argued that isotopic composition of CAS is sufficiently buffered against isotopic exchange (Gill et al., 2007; Lyons et al., 2004). Therefore, the studied samples have most likely preserved their primary carbon and sulfur isotope compositions.

6.4 Post-LJE negative carbon isotope excursions: a local or global signal?

The carbon isotopic composition of carbonate and OM can provide insights into the oceanic carbon reservoir, which is linked to the redox state of the ocean and the atmosphere (Ossa Ossa, 2018). Carbonates from the Huaiyincun Formation show roughly synchronous variation in both $\delta^{13}C_{carb}$ and $\delta^{13}C_{org}$ values, which suggests that the carbonate and organic carbon was likely from the same dissolved inorganic carbon (DIC) reservoir. The significant decrease of $\delta^{13}C_{carb}$ values from -0.1‰ to -3.7‰ is observed between 65.6m and 82.5m, sandwiched between a lower part with $\delta^{13}C_{carb}$ values around 0‰ and an upper part with $\delta^{13}C_{carb}$ values around -3‰. Similar transition from 0‰ to a few permil negative values of $\delta^{13}C$ can be found in modern seawater with the increase of water depth. In the modern Pacific Ocean, $\delta^{13}C$ value of DIC in surface seawater is around +2‰ and gradually decreases to about -1‰ at 1000m depth (Kroopnick, 1985). Larger gradient of $\delta^{13}C$ value could be maintained if a stable chemocline was present, separating oxic surface water from deep anoxic water (Jiang et al., 2007). In the Black Sea, a gradual decrease of $\delta^{13}C$ up by 7‰ has been documented from the surface water to 2100-2200m depth (Deuser, 1970; Fry et al., 1991). In the Huaiyincun environment, the change in water depth was apparently too small to create a $\delta^{13}C$ gradient of -3‰. Furthermore, the abrupt increase in water depth at 91.6m as manifested by the transition from hematite- and detrital-rich carbonates to the relatively organic-rich carbonates clearly postdate the onset of the decline in $\delta^{13}C_{carb}$ at 65.6m. Thus, it is unlikely that the negative $\delta^{13}C_{carb}$ excursion in the Huaiyincun Formation represents the local depth gradient of seawater C isotope ($\delta^{13}C_{DIC}$).

A few other processes can decrease the seawater $\delta^{13}C_{carb}$ signature, including oxidation of previously deposited OM (e.g., Kump et al., 2011). Anaerobic oxidation of methane (AOM) can also generate carbonates with negative $\delta^{13}C_{carb}$, (Hayes and Waldbauer, 2006; Iudovich et al., 1990). Dolostones with

negative $\delta^{13}C_{carb}$ in the Huaiyincun Formation is unlikely related to AOM because it would produce carbonates with $\delta^{13}C_{carb}$ values much lower than -3‰ (Jiang et al., 2003) or higher than +15‰ (Dix et al., 1995), along with OM with $\delta^{13}C_{org}$ < -29‰ (Hayes, 1994).

Considering the age of the Huaiyincun Formation which was constrained between 2.0-1.9Ga, the slightly positive to near-zero $\delta^{13}C_{carb}$ values of carbonates in the lower Huaiyincun Formation and the underlying successions (the Daguandong, Jianancun, Hebiancun formations) (She et al., 2016) likely correspond to the aftermath of the LJE. During the LJE, the flourishing primary productivity as photoautotrophic bacteria followed by the rise of oxygen level provided abundant biomass with $\delta^{13}C_{org}$ lower than -20‰, the burial of which led to the largest ever positive $\delta^{13}C$ excursions in coeval seawater (Martin et al., 2013a). This event was thought to have ended as the $\delta^{13}C$ values in sediments returned to around 0‰ at ca. 2060Ma (Martin et al., 2013b). Nevertheless, a negative $\delta^{13}C$ excursion in carbonates and shales occurred shortly after the LJE, with $\delta^{13}C_{carb}$ down to -13.4‰, which was interpreted as a signal of the re-oxidation of the OM generated in the preceding LJE (Kump et al., 2011). Regional methanotrophy could also explain the negative shift of $\delta^{13}C_{org}$ (Qu et al., 2012). The decline in $\delta^{13}C_{carb}$ at 65.6-82.5m of the Huaiyincun Formation is consistent with those in other successions in the Post-LJE (Fig. 8), including the 2090 to 1980 Ma Zaonega Formation in Russia, with a drop from about +5‰ to < -10‰ (Kump et al., 2011), and the negative carbon isotope excursion in ~2.05Ga Francevillian Group (Ossa Ossa et al., 2018). Although a distinct large-step negative $\delta^{13}C$ excursion of about 14% occurs reported in the Zaonega Formation (Kump et al., 2011), part of the carbonate samples were thought to have been altered by post-depositional processes (Črne et al., 2014). Melezhik et al. (2015) reviewed the database of the Zaonega Formation and convincingly recognized the least altered $\delta^{13}C_{carb}$ values ranging from about +5‰ to about -5‰. The minor differences in amplitude of the negative excursion among these three localities reveal the spatial and temporal heterogeneity of $\delta^{13}C$ variations of post-LJE. The relatively small $\delta^{13}C$ excursion (-3.6‰) in the Huaiyincun Formation seems likely to represent the signature of the global DIC reservoir although more $\delta^{13}C$ data from coeval carbonates is needed to support this hypothesis. The Huaiyincun Formation thus lends support to the view that this negative carbon isotope excursion was a global or at least a multi-basinal phenomena with variable local records. Such a widespread negative $\delta^{13}C$ excursion would require oxidation of large quantities of OM if contemporaneously occurring in several basins and hence a drawdown of the atmospheric and oceanic oxygen level.

6.5 Contraction and recovery of the marine sulfate reservoir

Sulfate evaporites deposited on carbonate platforms during the LJE provide solid evidence for the expansion of SSR(Bekker and Holland, 2012). Narrow range of $\delta^{34}S$ values and ubiquitous presence of evaporitic sulfate deposition from this interval have shown that the contemporaneous sulfate level of seawater ($[SO_4^{2-}]_{sw}$) reached a sizeable value (Blättler et al., 2018; Melezhik et al., 2005; Planavsky et al., 2012; Préat et al., 2011; Reuschel et al., 2012; Schröder et al., 2008). A recent study on the ~2.1 Ga evaporites in the Tulomozero Formation of the Onega Basin, Russian Karelia further documented the presence of a substantial oxidant reservoir (> 10 mM) in the form of marine sulfate (Blättler et al., 2018). In the Dashiling Formation of the Doucun Group, however, abundant halite pseudomorphs have been observed whereas no gypsum (pseudomorphs) was reported (Bai, 1986). This suggests that the Hutuo Supergroup probably witnessed the contracted marine sulfate reservoir at the termination of the LJE.

Several methods have been used to constrain the $[SO_4^{2-}]_{sw}$ in the geological history, including CAS concentration. Although CAS is considered unlikely to be an unambiguous quantitative proxy for the marine sulfate reservoir due to its vulnerable nature and diagenetic loss (Gill et al., 2008), it has been shown that CAS concentration in carbonates may record temporal variations of the sulfate reservoir (Habicht et al., 2002; Kah et al., 2004; Planavsky et al., 2012). The CAS concentrations in the Huaiyincun dolostones (<28.1 ppm) are significantly lower than those in the LJE interval (177-232 ppm) (Planavsky et al., 2012), even lower than those in the Mesoproterozoic (Luo et al., 2015), which supports a substantial decrease of the marine sulfate concentration to an extremely low level.

To better constrain the size of the post-LJE seawater sulfate reservoir, we quantified the $[SO_4^{2-}]_{sw}$ using the "rate method" developed by Algeo et al. (2015), which is based on the difference in S-isotope fractionations between co-occurring sulfate and sulfide ($\Delta^{34}S_{CAS\text{-}py}$) and the observed maximum rate of $\delta^{34}S_{CAS}$ variation ($\partial\delta^{34}S_{CAS}/\partial t$, where t is time) (See Algeo et al., 2015, for details). These two parameters can be related to each other through a function: $[SO_4^{2-}]_{sw}$ (max)=$k_1 \times k_2 \times F_{PY} \times \Delta^{34}S_{CAS\text{-}PY}/(\partial\delta^{34}S_{CAS}/\partial t)$ (max), where F_{PY} represent the burial flux of reduced sulfur (mainly pyrite), k_1 and k_1 is constantly equal to 10^6 and 2.22×10^{-20} mM g^{-1}, respectively (Algeo et al., 2015). Due to the absence of sulfide (pyrite) in the Huaiyincun dolostones, we used the average $\Delta^{34}S_{CAS\text{-}py}$ value of 19.5‰ in the interval from 2.0 to 1.9Ga (compiled by Luo et al., 2015). The duration of the 4657m succession which consist of the Jianancun, Daguandong, Huaiyincun, Beidaxing and Tianpengnao was estimated to be 110 Myrs based on the age data derived from the overlying Guojiazhai Group (1.9-1.8Ga) and the underlying Hebiancun Group (<2010Ma) (Bai, 1986; Liu et al., 2011). This analysis yielded sedimentation rate of around 42m/Myr. The change rates of $\partial\delta^{34}S_{CAS}$ were calculated within every four data, as the quotient of $\Delta^{34}S_{(n+4)\text{-}n}$ and duration. These consequently yielded the $\partial\delta^{34}S_{CAS}/\partial t$ (max) of 50.3‰ /Myr in the Huaiyincun Formation. Note that we required a minimum of 4 points to define a S-isotopic shift, shifts within 2 or 3 points were ignored to avoid the outliners. Calculation of the $[SO_4^{2-}]_{sw}$ for the Huaiyincun Formation yielded the maximum value of 0.3 mM for an oxic ocean (F_{PY} is about 4×10^{13}g yr^{-1}) and 0.8 mM for an anoxic ocean (F_{PY} is about 10×10^{13}g yr^{-1}) (Fig. 9). This low $[SO_4^{2-}]_{sw}$ suggests a significant contraction of the SSR following the LJE. The remarkably low level of $[SO_4^{2-}]_{sw}$ after the LJE is supported by the absence of sulfate in evaporites at ~1.9 Ga (Pope and Grotzinger, 2003; Grotzinger et al., 1993) and the occurrence of a fundamental change in the sedimentary sulfur isotopic composition (Och and Shields-Zhou, 2012; Scott et al., 2014). Although pseudomorphs replacing sulfate crystals have been reported from younger Paleoproterozoic and Mesoproterozoic successions (e.g., 1.7–1.6 Ga sabkha deposits of the McArthur basin (Walker et al., 1977; McClay and Carlile, 1978), these are rare and do not form massive beds.

The high-resolution $\delta^{34}S_{CAS}$ data from the Huaiyincun Formation can provide further insight into the aftermath of the LJE. Two stages of $\delta^{34}S_{CAS}$ evolution are observed in the Huaiyincun carbonates. In the lower part ($\leq$ 65.6m), $\delta^{34}S_{CAS}$ shows fluctuation around +20‰, along with near-zero $\delta^{13}C_{carb}$, comparable with those in the modern surficial seawater (Kah et al., 2004). Neither of these two isotope systematics shows significant shift within the 65.6m-thick proportion of the lower Huaiyincun Formation. This steady state ends by a prominent decline in $\delta^{34}S_{CAS}$ above 65.6m which is followed by a second stage of the curve with lower values. Like the negative $\delta^{13}C_{carb}$ excursion, this decline in $\delta^{34}S_{CAS}$ can not be explained by decreased local detrital input from continental weathering or increased seawater depth, but rather represents purturbations in the sulfur cycling probably related to the decreased pyrite burial or/and enhanced continental sulfide weathering.

493 *6.6 Transition to the SFE*

494 It has been proposed that the first-order variations in atmospheric oxygen, ocean redox state, and
495 the size of the SSR are directly related, as supported by the coincidence of the rise of SSR and the GOE
496 and the initiation of the LJE (Scott et al., 2014). In the Hutuo Supergroup, oscillating positive and
497 negative $\delta^{13}C_{carb}$ values in ~3,000 m thick carbonates underlying the Huaiyincun Formation was
498 interpreted as the aftermath of the LJE (She et al., 2016). Assuming a sedimentation rate of 40 m/Myr
499 for Proterozoic successions (Kah et al., 2004), this interval represents a period of ~75Myrs that
500 characterize the prolonged transition from the LJE to the SFE. In response to the termination of the LJE,
501 the SSR appears to have decreased significantly, as evidenced by the demise of massive sulfate evaporite
502 deposits (Pope and Grotzinger, 2003), $\delta^{34}S$ of sulfate and CAS (Planavsky et al., 2012), and highly ^{34}S-
503 depleted pyrites (Scott et al., 2014). The modelled $[SO_4^{2-}]_{sw}$ (<0.8 mM) and the extremely low CAS
504 concentration for all the Huaiyincun dolostones suggest that the contraction of the SSR probably
505 happened before the deposition of this formation.
506 Seawater S-isotopic composition is mainly equilibrated by the flux of weathering-derived sulfate to
507 the ocean and the flux of sulfur exported from the oceans through the burial of sulfide and sulfate (Bottrell
508 and Newton, 2006).The decrease in $\delta^{34}S_{CAS}$ values and the absence of sulfide (pyrite) in the Huaiyincun
509 Formation can be related to the inhibition of bacteria sulfate reduction, which is consistent with carbonate
510 deposition and early diagenesis in a well-oxidized shallow ocean, or to decreased pyrite burial or/and
511 enhanced continental sulfide weathering. In the upper Huaiyincun Formation, however, there is clearly
512 an increasing trend of CAS concentration (Fig. 6), possibly suggesting a slight expansion of the seawater
513 sulfate reservoir. This, however, did not result in the return of seawater sulfate concentrations to early
514 Paleoproterozoic levels, as documented by the overall low CAS concentrations in the Huaiyincun and
515 other post-LJE carbonates. This change can be attributed to enhanced continental weathering or/and
516 sulfide oxidation. Without a coeval increase in gypsum burial, both processes would have inevitably led
517 to an expansion of the SSR. Tectonic processes like the breakup of the Paleoproterozoic supercontinent
518 might have provided extra fresh rocks exposed to the atmospheric oxygen, therefore enhancing
519 continental weathering. Nevertheless, it was not until late Neoproterozoic did the seawater sulfate
520 concentrations return to $\geq$ 2.5mM (Scott et al., 2014). In summary, the present study highlights a critical
521 transition to the SFE that recorded dynamic carbon and sulfur cycles in the aftermath of the LJE.
522
523 **Conclusions**
524 Carbonates in the 2.0-1.9 Ga Huaiyincun Formation of the Hutuo Supergroup are well preserved and
525 have only been metamorphosed to the sub-greenschist facies. The lower Huaiyincun Formation, often
526 containing imbricated edgewise intraclasts and showing hummocky cross-stratification, are
527 characterized by pink-purple dolostones enriched in hematite and detrital minerals, while the upper
528 Huaiyincun Formation is dominated by normally graded grey-clored intraclastic dolostones with
529 distinctly lower detrital contents and higher organic content. These features suggest a transgression
530 during the deposition of the Huaiyincun Formation.
531 In the ~200-m thick Huaiyincun Formation, transition from dolostone rich in hematite and detrital
532 minerals to those with less detrital phases and hematite is observed at 91.6m above the base. Whereas
533 the onset of negative $\delta^{13}C_{carb}$ and $\delta^{34}S_{CAS}$ excursions is observed at 65.6m. The unsynchronized changes
534 between mineral assemblage and C, S-isotopic systematics suggest that change in water depth during

transgression has negligible impact on the $\delta^{34}S_{CAS}$ and $\delta^{13}C_{carb}$ values. The negative $\delta^{13}C_{carb}$ excursion from -0.1‰ to -3.7‰ in the Huaiyincun Dolostones was therefore resembling with those in Gabon and Russia, as part of a multi-basinal phenomenon that may have been global. Such a widespread negative $\delta^{13}C$ excursion would require oxidation of large quantities of OM and hence a drawdown of the atmospheric and oceanic oxygen level.

The high variability of $\delta^{34}S_{CAS}$ values ranging from 33.1% to -1.2‰ and the low CAS concentration of the carbonates in the Huaiyincun Formation reveal an extremely low seawater sulfate level after the LJE. Modelling based on the values of $\partial\delta^{34}S_{CAS} / \partial t$ and $\delta^{34}S_{CAS\text{-}py}$ further suggests the $[SO_4^{2-}]_{sw}$ might be less than 0.8 mM. The decrease in $\delta^{34}S_{CAS}$ and the increase of CAS concentration in the upper Huaiyincun Formation, however, probably represent a slight expansion of the seawater sulfate reservoir related to elevated sulfate flux by oxidative continental weathering.

Acknowledgements

· We would like to acknowledge funding from National Natural Science Foundation of China (grant# 41272038, 41472170, 41825019 and 41821001), Strategic Priority Research Program of Chinese Academy of Sciences (grant# XDB26020102), and State Key Laboratory of Biogeology and Environmental Geology, China University of Geosciences (grant# GBL11801). We thank Zihu Zhang for his help on the CAS analysis and Shuzhan Liu for his assistance in field work and sample preparation. Matthew S. Dodd provided helpful discussion and improved an earlier version of the manuscript.

References

Algeo, T.J., Luo, G.M., Song, H.Y., Lyons, T.W., Canfield, D.E., 2015. Reconstruction of secular variation in seawater sulfate concentrations. Biogeosciences 12, 2131–2151.

Baker, A.J., Fallick, A.E., 1989a. Evidence from Lewisian limestones for isotopically heavy carbon in two-thousand-million-year-old sea water. Nature 337, 352-354.

Baker, A.J., Fallick, A.E., 1989b. Heavy carbon in two-billion-year-old marbles from Lofoten-Vester□len, Norway: Implications for the Precambrian carbon cycle. Geochim. Cosmochim. Acta 53, 1111-1115.

Banner, J.L., Hanson, G.N., 1990. Calculation of simultaneous isotopic and trace element variations during water-rock interaction with applications to carbonate diagenesis. Geochim. Cosmochim. Acta 54, 3123–3137.

Bekker, A., Holland, H.D., 2012. Oxygen overshoot and recovery during the early Paleoproterozoic. Earth Planet. Sci. Lett. 317–318, 295–304.

Bekker, A., Karhu, J.A., Eriksson, K.A., Kaufman, A.J., 2003. Chemostratigraphy of Paleoproterozoic carbonate successions of the Wyoming Craton tectonic forcing of biogeochemical change. Precambr. Res. 120.

574 Bekker, A., Karhu, J.A., Kaufman, A.J., 2006. Carbon isotope record for the onset of the Lomagundi
575 carbon isotope excursion in the Great Lakes area, North America. Precambr. Res. 148, 145–180.

576 Berner, R.A., 1989. Biogeochemical cycles of carbon and sulfur and their effect on atmospheric oxygen
577 over Phanerozoic time. Palaeogeogr., Palaeoclimatol., Palaeoecol. (Global Planet. Change Sect.),
578 75, 97-122.

579 Beyssac, O., Goffe, B., Chopin, C., Rouzaud, J.N., 2002. Raman spectra of carbonaceous material in
580 metasediments: a new geothermometer, J. Met. Geol. 20, 859– 871.

581 Beyssac, O., Goffé, B., Petitet, J.P., Froigneux, E., Moreau, M., Rouzaud, J.N., 2003. On the
582 characterization of disordered and heterogeneous carbonaceous materials by Raman spectroscopy.
583 Spectrochim. Acta Part A. 59, 2267–2276.

584 Bickle, M.J., Chapman, H.J., Ferry, J.M., Rumble, D., Fallick, A.E., 1997. Fluid Flow and Diffusion in
585 the Waterville Limestone, South—Central Maine: Constraints from Strontium, Oxygen and
586 Carbon Isotope Profiles. J. Petrol. 38, 1489-1512.

587 Blättler, C.L., Claire, M.W., Prave, A.R., Kirsimäe, K., Higgins, J.A., Medvedev, P. V., Romashkin,
588 A.E., Rychanchik, D. V., Zerkle, A.L., Paiste, K., Kreitsmann, T., Millar, I.L., Hayles, J.A., Bao,
589 H., Turchyn, A. V., Warke, M.R., Lepland, A., 2018. Two-billion-year-old evaporites capture
590 Earth's great oxidation. Science 360, 320–323.

591 Bottrell, S.H., Newton, R.J., 2006. Reconstruction of changes in global sulfur cycling from marine sulfate
592 isotopes. Earth-Science Rev. 75, 59–83.

593 Brasier, A.T., Fallick, A.E., Prave, A.R., Melezhik, V.A., Lepland, A., 2011. Coastal sabkha dolomites
594 and calcitised sulphates preserving the Lomagundi-Jatuli carbon isotope signal. Precambr. Res.
595 189, 193–211.

596 Canfield, D.E., Teske, A., 1996. Late Proterozoic rise in atmospheric oxygen concentration inferred from
597 phylogenetic and sulphur-isotope studies. Nature 382, 127-132.

598 Chen, Y., Chen, W., Li, Q., Santosh, M. and Li, J., 2019. Discovery of the Huronian Glaciation Event in
599 China: Evidence from glacigenic diamictites in the Hutuo Group in Wutai Shan. Precambr.
600 Res. 320, 1-12.

601 Cleveland, W.S., Grosse, E., Shyu, W.M., 1992. Local regression models Statistical models in S, 309–
602 376.

603 Coplen, T.B., Kendall, C., Hopple, J., 1983. Comparison of stable isotope reference sample [J]. Nature
604 302, 236-238.

605 Črne, A. E., Melezhik, V. A., Lepland, A., Fallick, A. E., Prave, A. R., Brasier, A. T., 2014. Petrography
606 and geochemistry of carbonate rocks of the Paleoproterozoic Zaonega Formation, Russia:
607 Documentation of ^{13}C-depleted non-primary calcite. Precambr. Res. 240, 79-93.

608 Deuser, W.G., 1970. Carbon-13 in black sea waters and implications for the origin of hydrogen sulfide.
609 Science 168 (3939), 1575-1577.

610 Dix, G.R., Thomson, M.L., Longstaffe, F.J., McNutt, R.H., 1995. Systematic decrease of high $\delta^{13}C$
611 values with burial in late Archaean (2.8 Ga) diagenetic dolomite: evidence for methanogenesis
612 from the Crixas Greenstone Belt, Brazil. Precambr. Res. 70, 253–268.

613 Dodd, M.S., Papineau, D., She, Z., Manikyamba, C., Wan, Y., O'Neil, J., Karhu, J., Rizo, H., Pirajno,
614 F., 2019. Widespread occurrences of variably crystalline ^{13}C-depleted graphitic carbon in banded
615 iron formations. Earth Planet. Sci. Lett. 512, 163-174.

616 Djokic, T., Kranendonk, M.J. Van, Campbell, K.A., Walter, M.R., Ward, C.R., 2017. Earliest signs of
617 life on land preserved in ca. 3.5 Ga hot spring deposits. Nat. Commun. 8, 1–8.

618 Du, L., Yang, C., Wyman, D.A., Nutman, A.P., Zhao, L., Lu, Z., Song, H., Geng, Y., Ren, L., 2017.
619 Zircon U-Pb ages and Lu-Hf isotope compositions from clastic rocks in the Hutuo Group: Further
620 constraints on Paleoproterozoic tectonic evolution of the Trans-North China Orogen. Precambr.
621 Res. 303, 291–314.

622 Du, L.L., Yang, C.H., Guo, J.H., Wang, W., Ren, L.D., Wan, Y.S., Geng. Y.S., 2010. The age of the
623 base of the Paleoproterozoic Hutuo Group in the Wutai Mountains area, North China Craton:
624 SHRIMP zircon U-Pb dating of basaltic andesite. Chinese Sci. Bull. 55, 1782–1789.

625 Du, L.L., Yang, C.H., Wang, W., Ren, L.D., Wan, Y.S., Song, H.X., Geng, Y.S., Hou, K.J., 2011. The
626 Re-examination of the age and stratigraphie subdivision of the Hutuo Group in the Wutai
627 Mountains area, North China craton: Evidence from geology and zircon U-pb geochronology. Acta
628 Petrol. Sin. 27, 1037–1055.

629 Fakhraee, M., Hancisse, O., Canfield, D.E., Crowe, S.A., Katsev, S., 2019. Proterozoic seawater sulfate
630 scarcity and the evolution of ocean–atmosphere chemistry. Nat. Geosci. 12(5), 375-380.

631 Fry, B., Jannasch, H.W., Molyneaux, S.J., Wirsen, C.O., Muramoto, J.A., King, S., 1991. Stable isotope
632 studies of the carbon, nitrogen and sulfur cycles in the Black Sea and the Cariaco Trench. Deep
633 Sea Res. Part A. Oceanogr. Res. Pap. 38, S1003–S1019.

634 Galimov, E.M., Kuznetsova, N.G., Prokhorov, V.S., 1968. On the problem of the Earth's ancient
635 atmosphere composition in connection with results of isotope analysis of carbon from the
636 Precambrian carbonates. Geochemistry 11, 1376-1381 (in Russian).

637 Gill, B.C., Lyons, T.W., Saltzman, M.R., 2007. Parallel, high-resolution carbon and sulfur isotope
638 records of the evolving Paleozoic marine sulfur reservoir. Palaeogeogr. Palaeoclimatol. Palaeoecol.
639 256, 156–173.

640 Gill, B.C., Lyons, T.W., Frank, T.D., 2008. Behavior of carbonate-associated sulfate during meteoric
641 diagenesis and implications for the sulfur isotope paleoproxy. Geochim. Cosmochim. Acta 72,
642 4699–4711.

643 Guo, H., Du, Y., Kah, L.C., Hu, C., Huang, J., Huang, H., Yu, W., Song, H., 2015. Sulfur isotope
644 composition of carbonate-associated sulfate from the Mesoproterozoic Jixian Group, North China:
645 Implications for the marine sulfur cycle. Precambr. Res. 266, 319–336.

Habicht, K.S., Gade, M., Thamdrup, B., Berg, P., Canfield, D.E., 2002. Calibration of sulfate levels in the Archean Ocean. Science 298 (5602), 2372–2374.

Hayes, J.M., 1994. Global methanotrophy at the Archean-Proterozoic transition. In: Bengtson, S. (Ed.), Nobel Symposium 84, Early life on Earth. Columbia University Press, New York, PP. 220-236.

Hayes, J.M., Waldbauer, J.R., 2006. The carbon cycle and associated redox processes through time. Philos. Trans. R. Soc. B Biol. Sci. 361, 931–950.

Holland H.D., 2002. Volcanic gases, black smokers, and the Great Oxidation Event. Geochim. Cosmochim. Acta 66, 3811–3826.

Hotinski, R.M., Kump, L.R., Arthur, M.A., 2004. The effectiveness of the Paleoproterozoic biological pump: a $\delta^{13}C$ gradient from platform carbonates of the Pethei Group (Great Slave Lake Supergroup, NWT). Geol. Soc. Am. Bull. 116, 539–554.

Iudovich, I.E., Makarikhin, V. V, Medvedev, P. V, Sukhanov, N. V, 1990. Carbon isotope anomalies in carbonates of the Karelian series. Geochemistry Int. 28, 972–978.

Jiang, G., Kennedy, M.J., Christie-Blick, N., 2003. Stable isotopic evidence for methane seeps in Neoproterozoic postglacial cap carbonates. Nature 426, 822–826.

Jiang, G., Kaufman, A.J., Christie-Blick, N., Zhang, S., Wu, H., 2007. Carbon isotope variability across the Ediacaran Yangtze platform in South China: Implications for a large surface-to-deep ocean $\delta^{13}C$ gradient. Earth Planet. Sci. Lett. 261, 303–320.

Kah, L.C., Lyons, T.W., Frank, T.D., 2004. Low marine sulphate and protracted oxygenation of the Proterozoic biosphere. Nature 431, 834–838.

Karhu, J.A., Holland, H.D., 1996. Carbon isotopes and the rise of atmospheric oxygen. Geology 24, 867–870.

Konhauser, K.O., Lalonde, S. V., Planavsky, N.J., Pecoits, E., Lyons, T.W., Mojzsis, S.J., Rouxel, O.J., Barley, M.E., Rosìere, C., Fralick, P.W., Kump, L.R., Bekker, A., 2011. Aerobic bacterial pyrite oxidation and acid rock drainage during the Great Oxidation Event. Nature 478, 369–373.

Kong, F.F., Yuan, X.L., Zhou, C.M., 2011. Paleoproterozoic glaciation: Evidence from carbon isotope record of the Hutuo Group, Wutai Mountain area of Shanxi Province, China. Chinese Sci. Bull. 56, 2922–2930.

Kroopnick, P.M., 1985. The distribution of ^{13}C of $\sum CO_2$ in the world oceans. Deep Sea Res. Part A Oceanogr. Res. Pap. 32, 57–84.

Kump, L.R., Junium, C., Arthur, M.A., Brasier, A., Fallick, A., Melezhik, V., Lepland, A., Črne, A.E., Luo, G., 2011. Isotopic Evidence for Massive Oxidation of Organic Matter Following the Great Oxidation Event. Science 334, 1694–1696.

Kusky, T.M., Li, J., 2003. Paleoproterozoic tectonic evolution of the North China Craton. J. Asian Earth Sci. 22, 383–397.

Li S., Xu S., Zhang J., Zhao Z., Wang D., Yang Y., Sun Z., Cao R., 1996. 1:50000 geological map of Dongye, China. Publicated by Geological Survey of Shanxi (In Chinese).

683 Lindsay, J.F., Brasier, M.D., 2002. Did global tectonics drive early biosphere evolution? Carbon isotope
684 record from 2.6 to 1.9 Ga carbonates of Western Australian basins, Precambr. Res. 114, 1-34.

685 Liu, C., Zhao, G., Sun, M., Zhang, J., He, Y., Yin, C., Wu, F., Yang, J., 2011. U-Pb and Hf isotopic study
686 of detrital zircons from the Hutuo group in the Trans-North China Orogen and tectonic implications.
687 Gondwana Res. 20, 106–121.

688 Luo, G., Kump, L.R., Wang, Y., Tong, J., Arthur, M.A., Yang, H., Huang, J., Yin, H., Xie, S., 2010.
689 Isotopic evidence for an anomalously low oceanic sulfate concentration following end-Permian
690 mass extinction. Earth Planet. Sci. Lett. 300, 101–111.

691 Luo, G., Ono, S., Huang, J., Algeo, T.J., Li, C., Zhou, L., Robinson, A., Lyons, T.W., Xie, S., 2015.
692 Decline in oceanic sulfate levels during the early Mesoproterozoic. Precambr. Res. 258, 36–47.

693 Luo, G., Ono, S., Beukes, N.J., Wang, D.T., Xie, S., Summons, R.E., 2016. Rapid oxygenation of
694 Earth's atmosphere 2.33 billion years ago. Sci. Adv. 2, e1600134–e1600134.

695 Lyons, T.W., Walter, L.M., Gellatly, A.M., Martini, A.M., Blake, R.E., 2004. Sites of anomalous organic
696 remineralization in the carbonate sediments of South Florida, USA: the sulfur cycle and car-
697 bonate-associated sulfate. Geol. Soc. Am. Spec. Pap. 379, 161–176.

698 Lyons, T.W., Reinhard, C.T., Planavsky, N.J., 2014. The rise of oxygen in Earth ' s early ocean and
699 atmosphere. Nature 506, 307–315.

700 Maheshwari, A., Sial, A.N., Gaucher, C., Bossi, J., Bekker, A., Ferreira, V.P., Romano, A.W., 2010.
701 Global nature of the Paleoproterozoic Lomagundi carbon isotope excursion: a review of
702 occurrences in Brazil, India, and Uruguay. Precambr. Res. 182, 274–299.

703 Marenco, P.J., Corsetti, F.A., Hammond, D.E., Kaufman, A.J., Bottjer, D.J., 2008. Oxidation of pyrite
704 during extraction of carbonate associated sulfate. Chem. Geol. 247, 124–132.

705 Martin, A.P., Condon, D.J., Prave, A.R., Lepland, A., 2013. A review of temporal constraints for the
706 Palaeoproterozoic large, positive carbonate carbon isotope excursion (the Lomagundi-Jatuli Event).
707 Earth-Science Rev. 127, 242–261.

708 Martin, A.P., Condon, D.J., Prave, A.R., Melezhik, V.A., Lepland, A., Fallick, A.E., 2013. Dating the
709 termination of the Palaeoproterozoic Lomagundi-Jatuli carbon isotopic event in the North
710 Transfennoscandian Greenstone Belt. Precambr. Res. 224, 160–168.

711 Mazumdar, A., Goldberg, T., Strauss, H., 2008. Abiotic oxidation of pyrite by Fe(III) in acidic media
712 and its implications for sulfur isotope measurements of lattice-bound sulfate in sediments. Chem.
713 Geol. 253, 30–37.

714 McClay, K.R., Carlile, D.G., 1978. Mid-proterozoic sulphate evaporites at Mount Isa mine, Queensland,
715 Australia. Nature 274, 240–241.

716 Melezhik, V.A., Fallick, Anthony E., Hanski, Eero J., Kump, Lee R., Lepland, Aivo, Prave, Anthony R.,
717 Strauss, H., 2005. Emergence of the aerobic biosphere during the Archean-Proterozoic transition:
718 Challenges of future research. GSA Today. 15, 11.

719 Melezhik, V.A., Fallick, A.E., 2010. On the Lomagundi-Jatuli carbon isotopic event: The evidence from
720 the Kalix Greenstone Belt, Sweden. Precambr. Res. 179, 165–190.

721 Melezhik, V.A., Fallick, A.E., Brasier, A.T., Lepland, A., 2015. Carbonate deposition in the
722 Palaeoproterozoic Onega basin from Fennoscandia: A spotlight on the transition from the
723 Lomagundi-Jatuli to Shunga events. Earth-Science Rev. 147, 65–98.

724 Och, L.M., Shields-Zhou, G.A., 2012. The Neoproterozoic oxygenation event: Environmental
725 perturbations and biogeochemical cycling. Earth-Science Rev. 110, 26–57.

726 Ossa Ossa, F., Eickmann, B., Hofmann, A., Planavsky, N.J., Asael, D., Pambo, F., Bekker, A., 2018.
727 Two-step deoxygenation at the end of the Paleoproterozoic Lomagundi Event. Earth Planet. Sci.
728 Lett. 486, 70–83.

729 Papineau, D., Mojzsis, S.J., Schmitt, A.K., 2007. Multiple sulfur isotopes from Paleoproterozoic
730 Huronian interglacial sediments and the rise of atmospheric oxygen. Earth Planet. Sci. Lett. 255,
731 188–212.

732 Papineau, D., She, Z., Dodd, M.S., 2017. Chemically-oscillating reactions during the diagenetic
733 oxidation of organic matter and in the formation of granules in late Palaeoproterozoic chert from
734 Lake Superior. Chem. Geol. 0–1.

735 Peng P., Zhai M.G., Zhang H.F., Guo J.H., 2005. Geochronological Constraints on the
736 Paleoproterozoic Evolution of the North China Craton: SHRIMP Zircon Ages of Different Types
737 of Mafic Dikes, Inter. Geol. Rev. 47, 492-508

738 Peng, P., Feng, L., Sun, F., Yang, S., Su, X., Zhang, Z., Wang, C., 2017. Dating the Gaofan and Hutuo
739 Groups – Targets to investigate the Paleoproterozoic Great Oxidation Event in North China. J.
740 Asian Earth Sci. 138, 535–547.

741 Planavsky, N.J., Bekker, A., Hofmann, A., Owens, J.D., Lyons, T.W., 2012. Sulfur record of rising and
742 falling marine oxygen and sulfate levels during the Lomagundi event. Proc. Natl. Acad. Sci. 109,
743 1–6.

744 Pope, M.C., Grotzinger, J.P., 2003. Paleoproterozoic Stark Formation, Athapuscow Basin, Northwest
745 Canada: Record of cratonic-scale salinity crisis. J. Sediment. Res. 73, 280–295.

746 Préat, A., Bouton, P., Thiéblemont, D., Prian, J.P., Ndounze, S.S., Delpomdor, F., 2011. Paleoproterozoic
747 high 13C dolomites from the Latoursville and Franceville basins (SE Gabon): Stratigraphic and
748 synsedimentary subsidence implications. Precambr. Res. 189, 212–228.

749 Qu, Y., Črne, A.E., Lepland, A. and Van Zuilen, M.A., 2012. Methanotrophy in a Paleoproterozoic oil
750 field ecosystem, Zaonega Formation, Karelia, Russia. Geobiology 10(6), 467-478.

751 Reuschel, M., Melezhik, V.A., Whitehouse, M.J., Lepland, A., Fallick, A.E., Strauss, H., 2012. Isotopic
752 evidence for a sizeable seawater sulfate reservoir at 2.1Ga. Precambr. Res. 192–195, 78–88.

753 Schidlowski, M., Eichmann, R., Junge, C.E., 1975. Precambrian sedimentary carbonates: carbon and
754 oxygen isotope geochemistry and implications for the terrestrial oxygen budget. Precambr. Res. 2,
755 1–69.

Schidlowski, M., Eichmann, R., Junge, C.E., 1976. Carbon isotope geochemistry of the Precambrian Lomagundi carbonate province, Rhodesia. Geochim. Cosmochim. Act. 40, 449–455.

Schröder, S., Bekker, A., Beukes, N.J., Strauss, H., van Niekerk, H.S., 2008. Rise in seawater sulphate concentration associated with the Paleoproterozoic positive carbon isotope excursion: Evidence from sulphate evaporites in the ~2.2-2.1 Gyr shallow-marine Lucknow Formation, South Africa. Terra Nov. 20, 108–117.

Scott, C., Wing, B.A., Bekker, A., Planavsky, N.J., Medvedev, P., Bates, S.M., Yun, M., Lyons, T.W., 2014. Pyrite multiple-sulfur isotope evidence for rapid expansion and contraction of the early Paleoproterozoic seawater sulfate reservoir. Earth Planet. Sci. Lett. 389, 95–104.

She, Z., Yang, F., Liu, W., Xie, L., Wan, Y., Li, C., Papineau, D., 2016. The termination and aftermath of the Lomagundi-Jatuli carbon isotope excursions in the Paleoproterozoic Hutuo Group, North China. J. Earth Sci. 27, 297–316.

Shi W, Li C, Luo G, Huang J, Thomas J. Algeo, Jin C, Zhang Z, Cheng M., 2018. Sulfur isotope evidence for transient marine-shelf oxidation during the Ediacaran Shuram Excursion. Geology 46, 267-270.

Song, H., Tong, J., Algeo, T.J., Song, H., Qiu, H., Zhu, Y., Tian, L., Bates, S., Lyons, T.W., Luo, G., Kump, L.R., 2014. Early Triassic seawater sulfate drawdown. Geochim. Cosmochim. Acta 128, 95–113.

Thompson, C.K., Kah, L.C., 2012. Sulfur isotope evidence for widespread euxinia and a fluctuating oxycline in Early to Middle Ordovician greenhouse oceans. Palaeogeogr. Palaeoclimatol. Palaeoecol. 313–314, 189–214.

Walker, R.N., Muir, M.D., Diver, W.L., Williams, N., Wilkins, N., 1977. Evidence of major sulphate evaporite deposits in the Proterozoic McArthur Group, Northern Territory, Australia. Nature 265, 526-529.

Wang, A., Dhamenincourt, P., Dubessy, J., Guerard, D., Landais, P., Lelaurain, M., 1989. Characterization of graphite alteration in an uranium deposit by micro-Raman spectroscopy, X-ray diffraction, transmission electron microscopy and scanning electron microscopy. Carbon N. Y. 27, 209–218.

Wan, Y., Dong, C., Wang, W., Xie, H., Liu, D., 2010. Archean Basement and a Paleoproterozoic Collision Orogen in the Huoqiu Area at the Southeastern Margin of North China Craton: Evidence from Sensitive High Resolution Ion Micro-Probe U-Pb Zircon Geochronology. Acta Geol. Sin. (English edition) 84, 91–104.

Wilde, S.A., Cawood, P.A., Wang, K., Nemchin, A., Zhao, G., 2004. Determining Precambrian crustal evolution in China: A case-study from Wutaishan, Shanxi Province, demonstrating the application of precise SHRIMP U-Pb geochronology. Geol. Soc. Spec. Publ. 226, 5–25.

Zhao, G., Wilde, S.A., Cawood, P.A., Sun, M., 2001. Archean blocks and their boundaries in the North China Craton: Lithological, geochemical, structural and P-T path constraints and tectonic evolution. Precambr. Res. 107, 45–73.

794 Zhong, H., Ma, Y.S., 1995. Discovery of early Proterozoic carbon isotope shift (in Chinese). Acta Geol.
795 Sin. 69, 186-190.

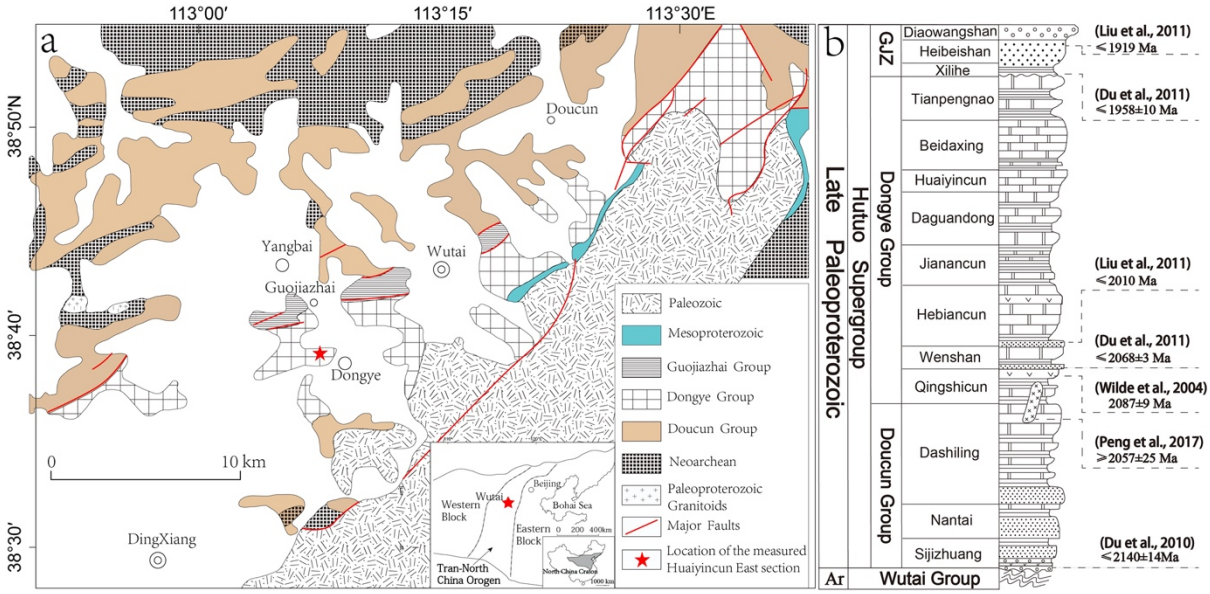

Figure. 1 Simplified geological map of the Wutai area (a, modified after Bai, 1986) and generalized stratigraphic column of the Hutuo Supergroup (b, modified after Bai, 1986) with previously published age data. Inset in a, tectonic framework of the North China Craton showing the study area. Ar, Archean; GJZ, Guojiazhai Group.

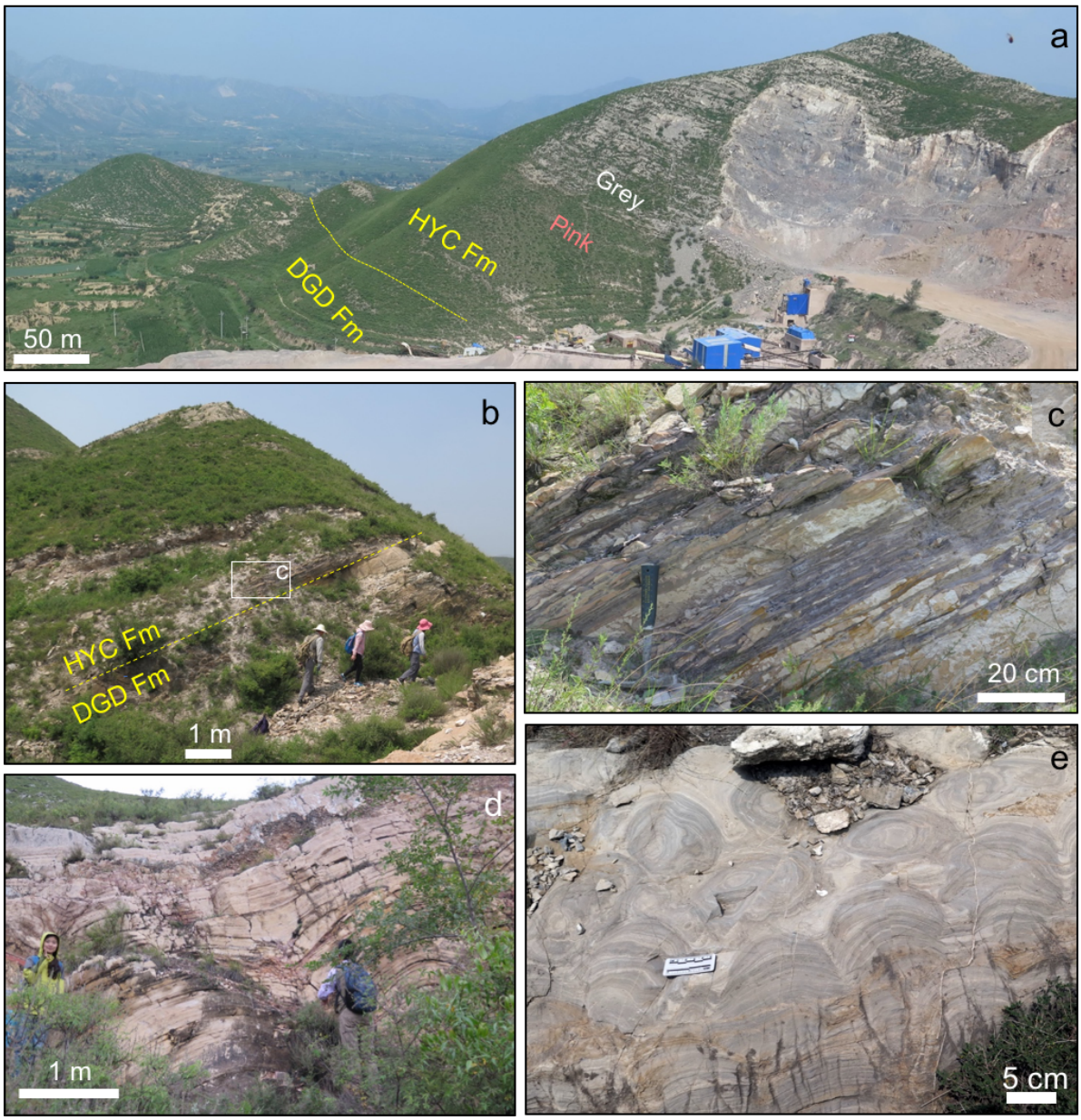

Fig. 2 Outcrops of the Daguangdong (DGD) and Huaiyincun (HYC) formations. a, The measured Huaiyincun East section showing the boundary between the two formations and the change in color of the Huaiyincun carbonates. Magnesium was being mined in the quarry. b, Closer view of the HYC/DG boundary. c, Medium bedded dolostone intercalated with purple metapelites near the base of the Huaiyincun Fm. (the marked area in b). d, A bed of meter-size stromatolitic bioherm near the base of the Huaiyincun Formation. e, Decimeter-size domal stromatolitic dolostone of the Daguandong Formation.

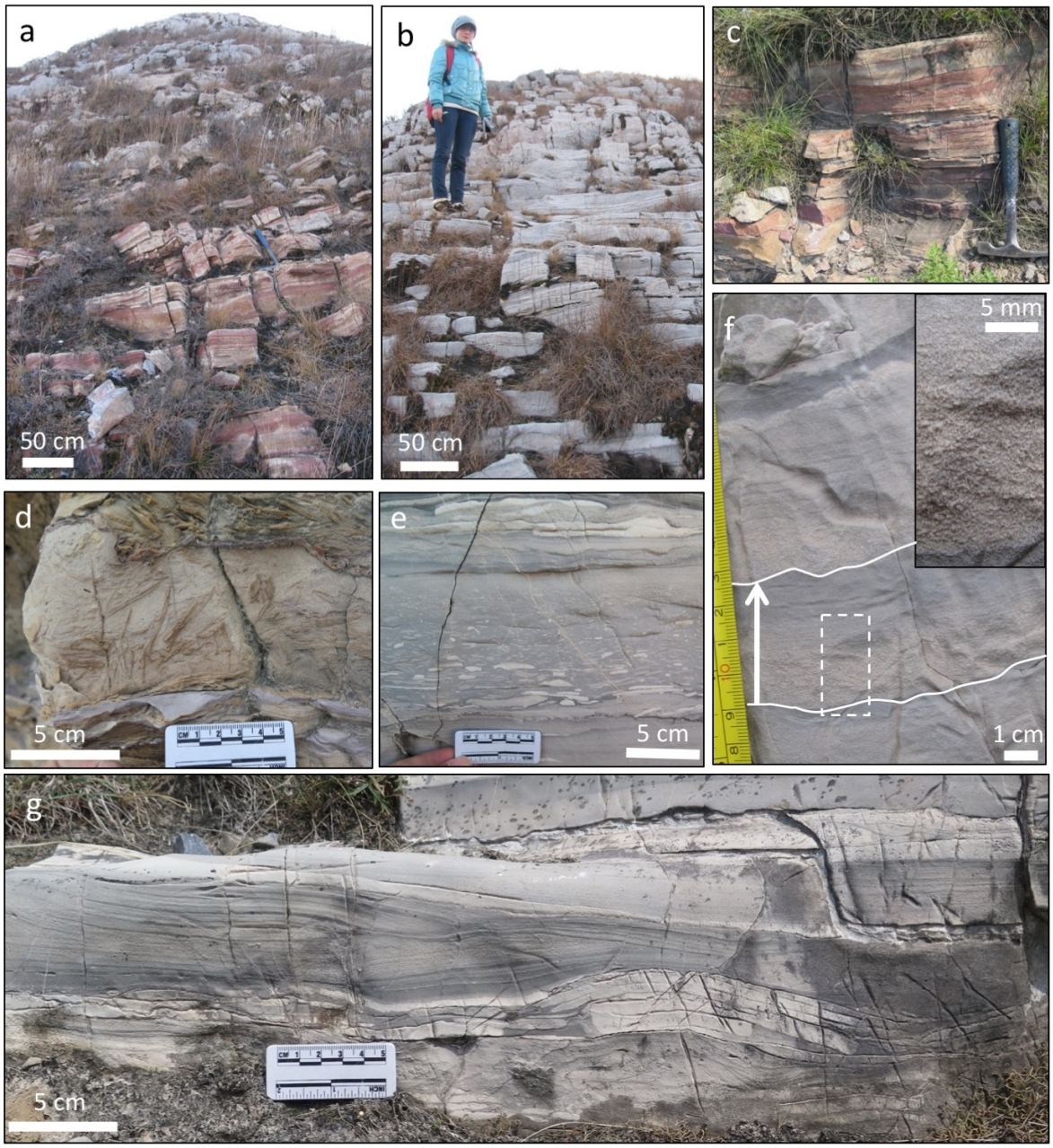

Fig. 3 Sedimentary structures of the Huaiyincun Fm. a, Transition from pink dolostones to grey dolostones. b, Grey dolostones of the upper Huaiyincun Formation. c, Pink banded dolostones. d, Imbricated edgewise intraclasts. e, Intraclastic dolostone showing normally graded bedding with a basal scour surface. f, Repeated cycles of normally graded (upward fining indicated by arrow) and laminated intraclastic dolostones, each starting from a basal scour surface (white lines). Inset in f, Closer view of sand-sized dolomitic intraclasts and graded bedding in the marked area. g, Decimeter-scale hummocky cross-stratification (HCS). c-d, Lower Huaiyincun Formation; e-g, Upper Huaiyincun Formation.

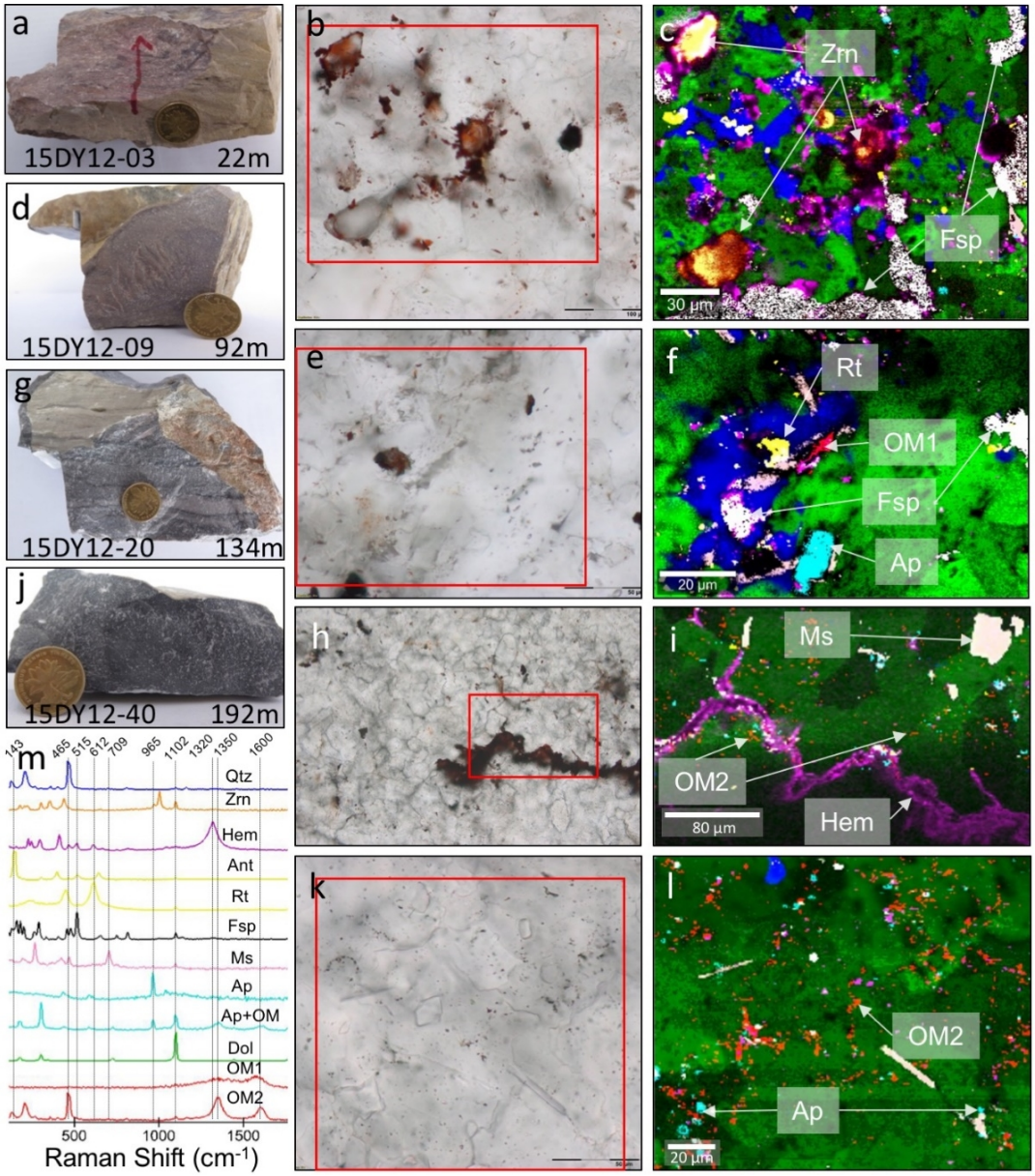

Figure 4 Hand specimen photos (a, d, g, j), photomicrographs (b, e, h, k; transmitted light, plane polarized) and Raman images (c, f, i, l) of representative samples. a, Hand specimen from 22m above the base; **b,** Photomicrograph of the sample in **a**; **c,** Raman image of the marked area in **b**, highlighting the zircon and feldspar crystals. **d,** Hand specimen from 91.6m; **e,** Photomicrograph of the sample in **d**; **f,** Raman image of the outlined area in **e**, showing type I OM (OM1), feldspar, rutile and large apatite grain. **g,** Hand specimen from 134m; **h,** Photomicrograph of the sample in **g**; **i,** Raman image of the marked area in **h**, showing muscovite, hematite and type II OM (OM2). **j**, Grey dolostone from 192m (upper Huaiyincun); **k,** Photomicrograph of the specimen in **j**; **l,** Raman image of the outlined area in **k**, note the higher abundance of organic matter (type II, OM2); **m,** Raman spectra of minerals highlighted in the Raman maps. Red boxes in **b**, **e**, **h** and **k** show the areas for Raman imaging in **c**, **f**, **i** and **l**. Color coding of the mineral phases in the Raman images: pink-muscovite (Ms), green-dolomite (Dol), white-feldspar (Fsp), orange-zircon (Zrn), yellow-titanium dioxide (rutile (Rt) and anatase (Ant)), purple-hematite (Hem), blue-quartz (Qtz), turquoise-apatite (Ap), red-organic matter (OM). Coins in a, d, g, j are 20mm in diameter.

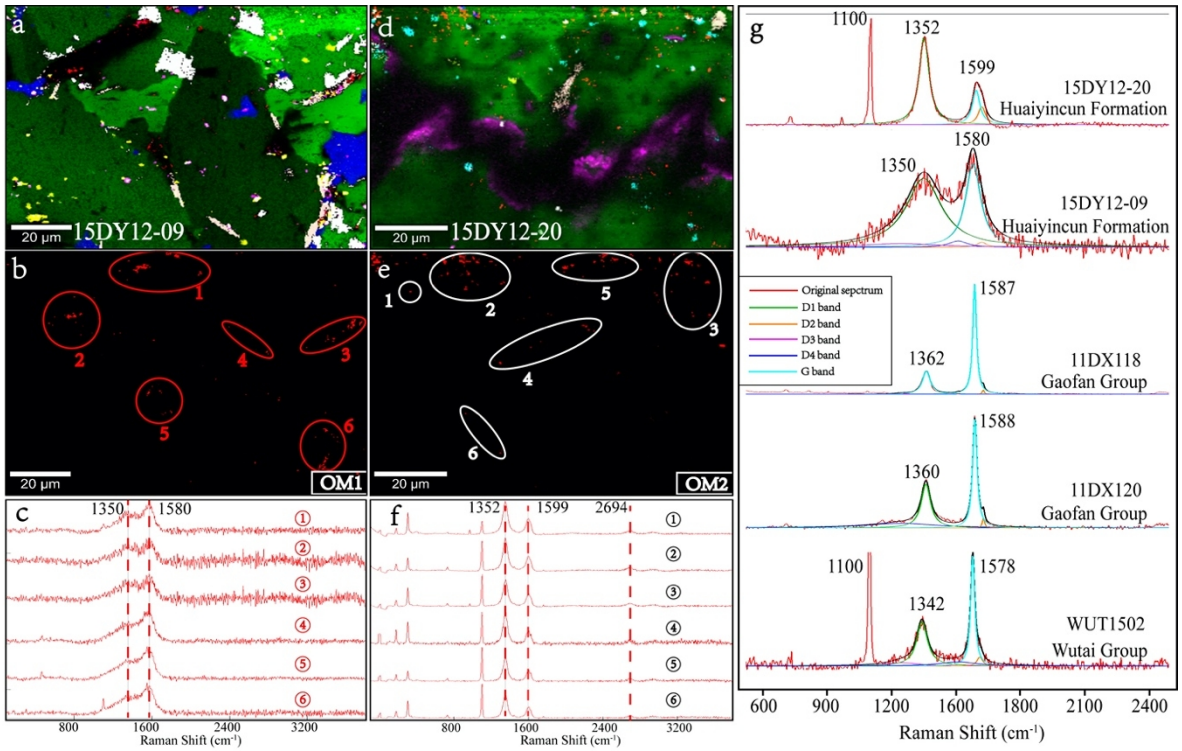

Figure 5 Raman images (a-b, d-e) and spectra (c, f) of two types of OM from the Huaiyincun Formation, compared with those of OM from the Gaofan and Wutai groups (g). **a,** Raman image of the dolostone (No.15DY12-09) at 91.6m of Huaiyincun Formation; **b,** Distribution of organic matter in sample 15DY12-09 showing the regions of interest where the Raman spectra in c were extracted; **c,** Raman spectra of selected organic matter in **b**; **d,** Raman image of the dolostone (No.15DY12-20) at 134m; **e,** Distribution of organic matter in sample 15DY12-20 showing the regions of interest where the Raman spectra in **f** were extracted. **f,** Raman spectra of selected organic matter in **e**. **g**, Comparison of Raman spectra with peak-fitting results. Color coding for minerals and organic matter: Pink-muscovite, green-dolomite, white-feldspar, yellow-titanium dioxide (rutile and anatase), purple-hematite, blue-quartz, turquoise-apatite, red-organic matter.

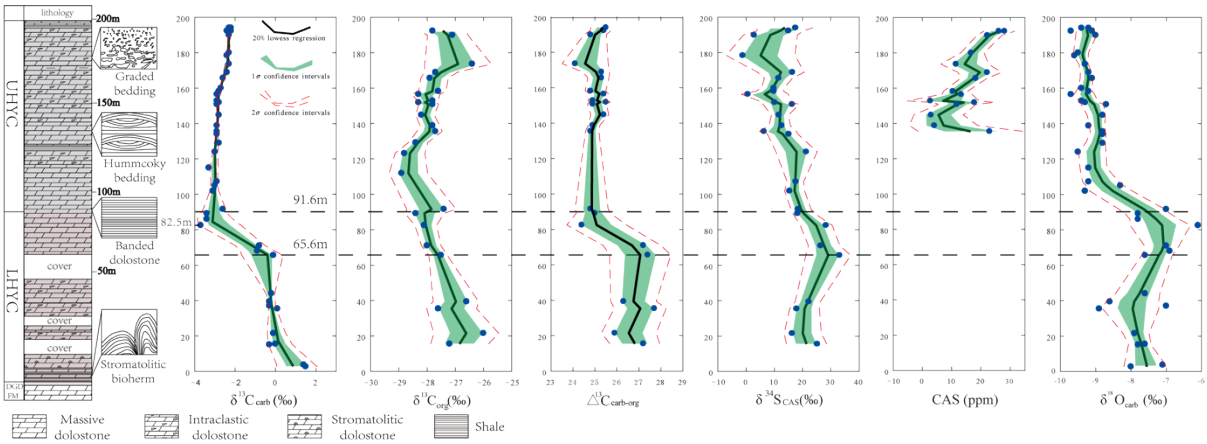

Figure 6 Stratigraphic variations of $\delta^{34}S_{CAS}$, $\delta^{13}C_{carb}$, $\delta^{18}O_{carb}$, $\delta^{13}C_{org}$ and total organic carbon (TOC) in the Huaiyincun Formation. The solid black line represents smoothed LOESS (locally weighted scatterplot smoothing), which determines a best-fit trend for irregularly distributed time-series data using an in- verse-distance-squared weight function (cf. Cleveland et al., 1992). The LOESS curves were calculated from $\delta^{13}C_{carb}$, $\delta^{13}C_{org}$, $\delta^{34}S_{CAS}$, [CAS] and $\delta^{18}O_{carb}$ data of the Huaiyincun Formation. 1σ confidence interval of the overall trend for each column is shaded in green. 2σ confidence intervals are shown in red dash line. LHYC, lower Huaiyincun Formation; UHYC, upper Huaiyincun Formation; DGD FM, Daguandong Formation. DM, decimeter-size domal stromatolite; HB, horizontal bedding; HCS, hummocky cross-stratification; GB, graded bedding. The stratigraphic column was colored according the color and mineralogy of the dolostones (i.e., enrichment or lack of hematite).

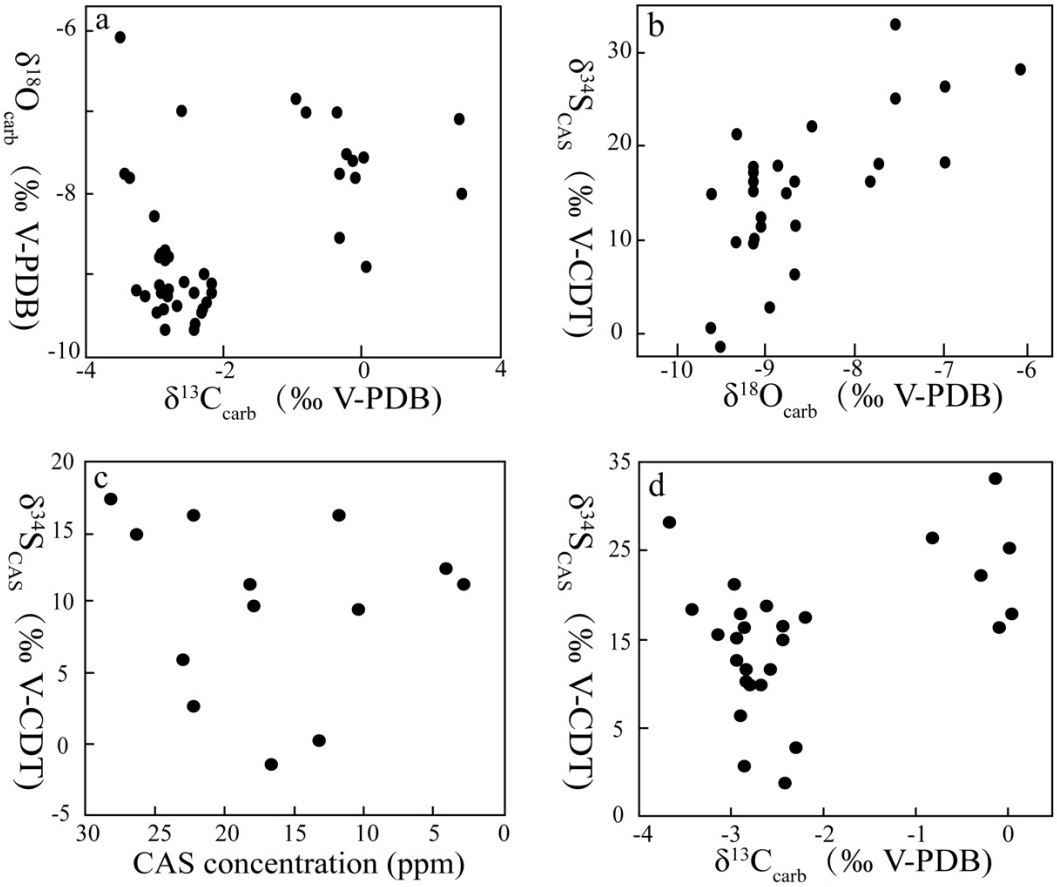

Figure 7 Cross plots of $\delta^{13}C_{carb}$ vs. $\delta^{18}O_{carb}$ (a), $\delta^{18}O_{carb}$ vs. $\delta^{34}S_{CAS}$ (b), CAS vs. $\delta^{34}S_{CAS}$ (c) and $\delta^{13}C_{carb}$ vs. $\delta^{34}S_{CAS}$ (d) for the Huaiyincun dolostones.

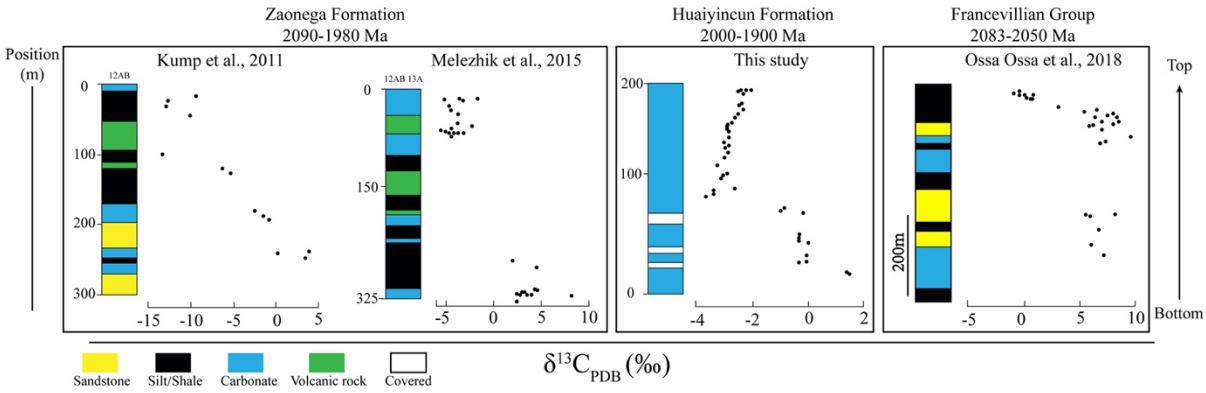

Figure 8 Negative excursions of $\delta^{13}C$ in carbonate successions at the LJE-SFE transition. Two groups of data of Zaonega Formation are shown because they are partly from samples in different drill cores. Data of Kump et al. (2011) all comes from samples in the drill cores No. 12A and 12B, whereas those of Melezhik et al. (2015) are from drill cores No. 12A and 12B and 13A. Data of the other successions are from outcrop samples.

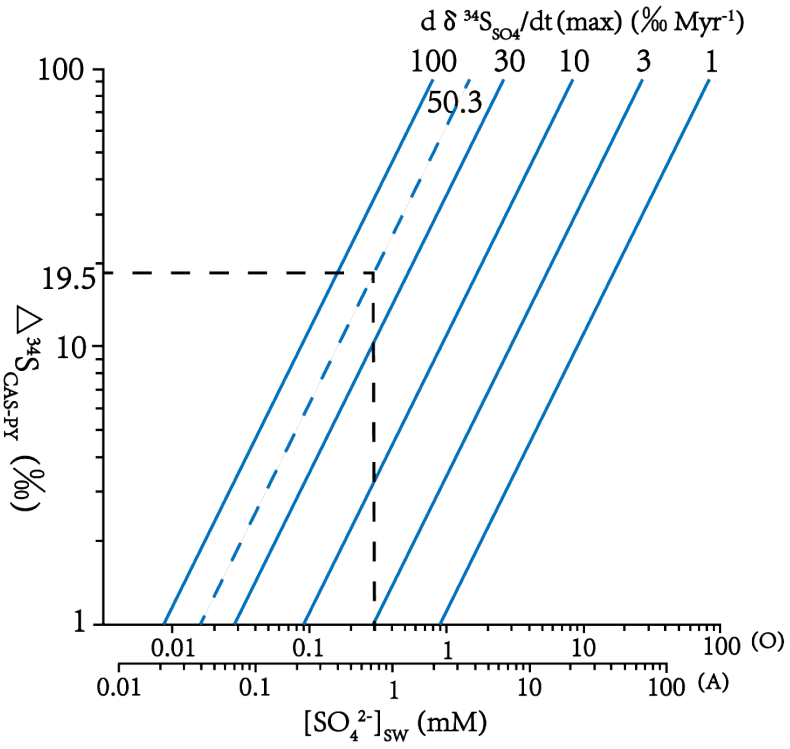

Figure. 9 Modelled seawater sulfate concentrations ($[SO_4^{2-}]_{sw}$) versus S-isotopic fractionation between sulfate and sulfide ($\delta^{34}S_{CAS-PY}$). The diagonal blue lines denote maximum rates of change in sulfate ($\partial\delta^{34}S_{CAS}/\partial t$) (max). The two scales on the x-axis represent $[SO_4^{2-}]_{sw}$ in oxic (O) and anoxic (A) oceans.

Table.1 Geochemical data of carbonates in the Huaiyincun Formation

Sample No.	Statigraphic Position (m)	$\delta^{13}C_{carb}$ (‰ V-PDB)	$\delta^{18}O_{carb}$ (‰ V-PDB)	$\delta^{18}O_{carb}$* (‰ V-SMOW)	$\delta^{34}S_{CAS}$ (‰ V-CDT)	$\delta^{13}C_{org}$ (‰ V-PDB)	TOC (wt%)	CAS (ppm)
11DX109-2	2.7	1.5	-8.0	22.6				
11DX109	3.7	1.4	-7.1	23.6				
11DX108	15.1	-0.3	-7.8	22.9				
15DY12-2	15.5	0.0	-7.6	23.1	25.2	-27.2	0.02	
15DY12-3	21.5	-0.1	-7.9	22.8	16.3	-26.0	0.01	
15DY12-4	35.4	0.1	-8.9	21.7	17.9	-27.6	0.01	
11DX107	37.0	-0.3	-7.0	23.7				
15DY12-5	39.4	-0.3	-8.6	22.1	22.2	-26.6	0.01	
11DX106	44.0	-0.2	-7.6	23.1				
15DY12-7	65.6	-0.1	-7.6	23.1	33.1	-27.5	0.02	
11DX105	68.0	-0.9	-6.9	23.8				
15DY12-8	71.0	-0.8	-7.0	23.7	26.4	-28.0	0.01	
15DY12-9	82.5	-3.7	-6.1	24.6	28.3	-28.1	0.02	
11DX104	86.0	-3.4	-7.8	22.9				
15DY12-10	89.2	-3.4	-7.8	22.9	18.2	-28.4	0.02	
15DY12-11	91.6	-2.6	-7.0	23.7	18.4	-27.4	0.02	
15DY12-13	101.9	-3.1	-9.3	21.4	15.4			
11DX102	105.0	-3.0	-8.3	22.4				
15DY12-14	107.2	-2.9	-9.2	21.4	17.6			
15DY12-15	111.9					-28.9	0.01	
11DX101	115.0	-3.3	-9.2	21.4				
15DY12-17	123.1					-28.8	0.02	
15DY12-18	124.0	-3.0	-9.5	21.2	21.3			
11DX100	129.0	-2.8	-8.8	21.8				
15DY12-19	129.2					-28.4	0.01	
15DY12-20	134.0	-2.9	-8.8	21.8	15.1			
15DY12-21	135.5	-2.9	-8.8	21.9	6.3	-27.7	0.01	22.96
15DY12-23	138.8	-2.9	-9.2	21.5	12.6	-27.8	0.01	4.11
15DY12-24	144.8	-2.8	-8.8	21.9	11.6	-28.2	0.01	2.97
15DY12-25						-28.5	0.02	
15DY12-26	150.8	-2.9	-8.7	21.9	16.3	-27.8	<0.01	11.77
15DY12-27	151.9	-2.8	-9.3	21.4	10.1	-28.3	0.01	17.79
15DY12-28	152.8	-2.9	-9.4	21.2		-27.8	0.01	2.76
15DY12-29	156.5	-2.9	-9.7	20.9	0.6	-28.3	0.01	13.25
15DY12-30	158.2	-2.8	-9.2	21.4	9.8	-27.6	0.01	10.41
15DY12-31	160.0	-2.7	-9.4	21.2	9.8			
15DY12-32	165.6	-2.6	-9.1	21.5	11.5	-27.9	<0.01	18.22
15DY12-33	168.9	-2.4	-9.2	21.4	16.4	-27.7	<0.01	22.15
15DY12-34	173.6	-2.3	-9.3	21.3		-26.4	<0.01	11.50
15DY12-35	178.4	-2.4	-9.6	21.0	-1.2			

15DY12-36	180.0	-2.3	-9.5	21.2				16.63
15DY12-38	189.9	-2.3	-9.0	21.6	2.8	-27.1	0.01	22.20
15DY12-39	192.3	-2.4	-9.7	20.9	15.0	-27.8	0.01	26.12
15DY12-39	192.3	-2.2	-9.1	21.5				28.09
15DY12-40	194.0	-2.2	-9.2	21.4	17.5	-27.7	0.01	
15DY12-40	194.0	-2.3	-9.4	21.2				

$\delta^{18}O_{carb}$ values were corrected assuming dolomite was the dominant carbonate mineral. $\delta^{18}O_{carb}$ -SMOW values were calculated according to the equation in Coplen et al., 1983.

Table 2. Parameters of the fitted Raman spectra for representatitive organic matter in the Huaiyincun Formation and the Gaofan Group and Wutai groups

Succession	Sample	Raman peak	Raman shift (cm-1)	FWHM	Peak Area	R^2	T ℃	Formula
Huaiyincun Formation	15DY12-20 (OM2)	D1	1352	51	3148	0.992	337	$T(℃) = -445 \times R + 641$ $R = [D1/(G + D1 + D2)]$ (Beyssac et al., 2002)
		D2	1625	20	146			
		D3	1245	100	200			
		D4	1510	100	100			
		G	1599	48	1314			
Huaiyincun Formation	15DY12-09 (OM1)	D1	1350	224	16951	0.966	327	
		D2	1620	19	244			
		D3	1245	160	798			
		D4	1510	110	2000			
		G	1580	79	6866			
Gaofan Group	11DX118	D1	1362	43	696	0.999	507	
		D2	1627	12	35			
		G	1587	20	1583			
Gaofan Group	11DX120	D1	1360	64	464	0.995	418	
		D2	1628	11	20			
		G	1588	25	440			
Wutai Group	WUT1502	D1	1342	60	983	0.956	424	
		D2	1612	30	100			
		G	1578	23	936			
		G	1599	48	1314			